Article

Cell

Architecture of Human Mitochondrial Respiratory Megacomplex $I_2III_2IV_2$

Graphical Abstract

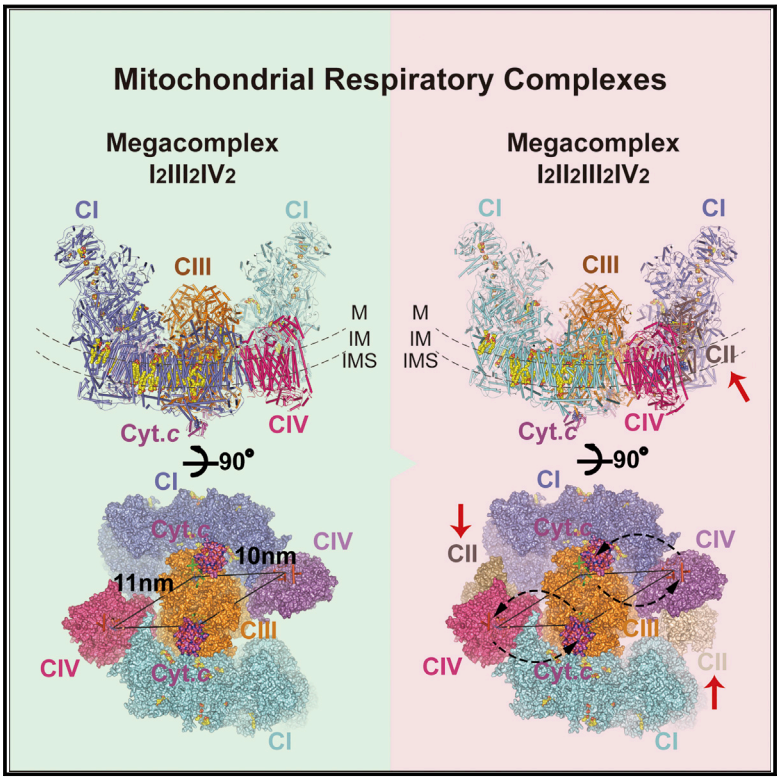

Authors

Runyu Guo, Shuai Zong, Meng Wu, Jinke Gu, Maojun Yang

Correspondence

maojunyang@tsinghua.edu.cn

In Brief

Structural analyses of the human respiratory supercomplex and megacomplex reveal the global arrangement of electron transport chain components, with implications for understanding the mechanism of electron transport.

Highlights

- Structure of human respiratory $SCI_1III_2IV_1$ and architecture of $MCI_2III_2IV_2$
- The atomic structures of human CI and CIII with side chains
- The $MCI_2III_2IV_2$ structure provides an alternative electron transfer mechanism
- CII can insert into the gaps between CI and CIV to form a closed ring of ETCS

Guo et al., 2017, Cell *170*, 1247–1257
September 7, 2017
http://dx.doi.org/10.1016/j.cell.2017.07.050

CellPress

Cell

Architecture of Human Mitochondrial Respiratory Megacomplex $I_2III_2IV_2$

Runyu Guo,[1,2] Shuai Zong,[1,2] Meng Wu,[1,2] Jinke Gu,[1,2] and Maojun Yang[1,3,*]
[1]Ministry of Education Key Laboratory of Protein Science, Tsinghua-Peking Joint Center for Life Sciences, Beijing Advanced Innovation Center for Structural Biology, School of Life Sciences, Tsinghua University, 100084 Beijing, China
[2]These authors contributed equally
[3]Lead Contact
*Correspondence: maojunyang@tsinghua.edu.cn
http://dx.doi.org/10.1016/j.cell.2017.07.050

SUMMARY

The respiratory megacomplex represents the highest-order assembly of respiratory chain complexes, and it allows mitochondria to respond to energy-requiring conditions. To understand its architecture, we examined the human respiratory chain megacomplex-$I_2III_2IV_2$ ($MCI_2III_2IV_2$) with 140 subunits and a subset of associated cofactors using cryo-electron microscopy. The $MCI_2III_2IV_2$ forms a circular structure with the dimeric CIII located in the center, where it is surrounded by two copies each of CI and CIV. Two cytochrome *c* (Cyt.*c*) molecules are positioned to accept electrons on the surface of the c_1 state CIII dimer. Analyses indicate that CII could insert into the gaps between CI and CIV to form a closed ring, which we termed the electron transport chain supercomplex. The structure not only reveals the precise assignment of individual subunits of human CI and CIII, but also enables future in-depth analysis of the electron transport chain as a whole.

INTRODUCTION

Mitochondria produce the majority of the energy carrier molecule ATP and function as the ''energy factory'' in the vast majority of cell types in the human body. The respiratory chain complexes (RCCs), containing four multi-subunit complexes (complex I–IV; CI, NADH:ubiquinone oxidoreductase; CII, succinate:ubiquinone oxidoreductase; CIII, cytochrome bc_1 complex; and CIV, cytochrome *c* oxidase), are located in the inner mitochondrial membrane and play important roles in energy conversion (Berrisford and Sazanov, 2009; Cogliati et al., 2013; Efremov et al., 2010; Iwata et al., 1998; Sánchez-Caballero et al., 2016; Schägger and Pfeiffer, 2000; Shinzawa-Itoh et al., 2016; Tsukihara et al., 1995, 1996; Vinothkumar et al., 2014; Zickermann et al., 2015). Among these complexes, CI is the entry point of electrons into RCCs and, together with CIII and CIV, couples electron transfer and proton translocation across mitochondrial inner membrane, leading to ATP synthesis by complex V (CV). In humans, dysfunctions of CI cause generation of reactive oxygen and nitrogen species. More importantly, CI dysfunction impairs oxidative phosphorylation, reduces the membrane potential and ATP synthesis, and leads to impaired NAD^+/NADH ratio. These defects perturb a large variety of metabolic processes and are implicated in a plethora of human diseases (Bakthavachalam and Shanmugam, 2017; Menezes et al., 2014; Rodenburg, 2016; Wirth et al., 2016), including Alzheimer's and Parkinson's diseases, multiple sclerosis, Friedreich's ataxia, amyotrophic lateral sclerosis, Hurthle cell thyroid carcinoma (HCTC), Leber's hereditary optic neuropathy (LHON), lethal infantile mitochondrial disease (LIMD), Leigh syndrome (LS), linear skin defects with multiple congenital anomalies 3 (LSDMCA3), mitochondrial encephalomyopathy with lactic acidosis and stroke-like episodes syndrome (MELAS), mitochondrial complex I deficiency (MT-C1D), and non-insulin-dependent diabetes mellitus (NIDDM), etc. Dysfunctions of CIII and CIV also cause severe human diseases (Fernández-Vizarra and Zeviani, 2015; Menezes et al., 2014; Rak et al., 2016), such as LHON, LS, histiocytoid cardiomyopathy 1, insulin-responsive hyperglycemia, mitochondrial complex III deficiency (MT-C3D), mitochondrial complex IV deficiency (MT-C4D), recurrent myoglobinuria (RM), Charcot-Marie-Tooth disease, microphthalmia with linear skin lesions (MLS), Björnstad syndrome, and GRACILE syndrome.

The RCCs have historically been deemed as separate enzymes (Enríquez, 2016). Schägger and Pfeiffer (2000) initially identified a higher integration level of respiratory chain complexes in blue native page (BN-PAGE) gels. The first fully functional respirasome was isolated from mouse, confirming this initial observation in blue native gels (Acín-Pérez et al., 2008). Most recently, our group reported a near-atomic resolution structure of respirasome ($SCI_1III_2IV_1$) from *Sus scrofa* (Gu et al., 2016; Wu et al., 2016), while two other groups reported medium resolution structures from *Ovis aries* and *Bos Taurus* (Letts et al., 2016; Sousa et al., 2016). Collectively, these studies also suggested the existence of higher order oligomerization of respiratory chain complexes (Letts et al., 2016; Wu et al., 2016). Based on rapid-freeze, deep-etch research of mitochondrial inner membrane, Schägger's group presented a model of respiratory strings based on the stoichiometry of CI–CIV. In their model, $I_2III_4IV_8$ form circular structures linked by III_2IV_4 to form a helical string along the cristae surface (Wittig et al., 2006b). Supporting this model, two groups later found megacomplex organization of CIII and CIV in yeast and bacteria (Heinemeyer et al., 2007; Sousa et al., 2013). However, the respiratory string

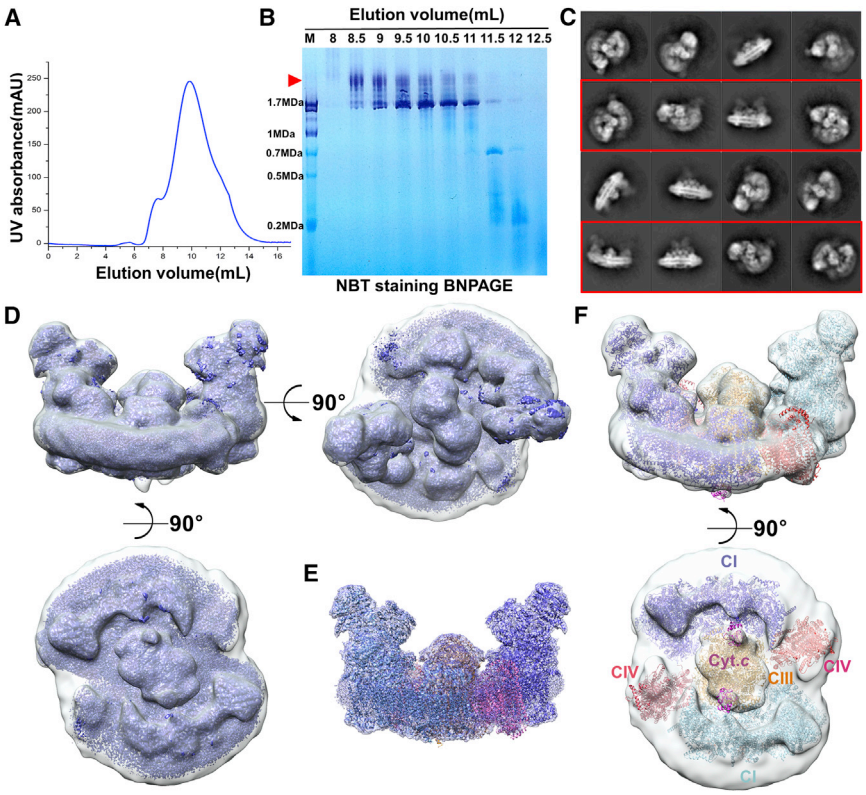

Figure 1. Biochemical Characterization and Overall Structure of Human $MCI_2III_2IV_2$

(A) A representative trace of size-exclusion chromatography of the respiratory chain supercomplexes by superose-6 (10/300 GL) column.

(B) Fractions of size-exclusion chromatography were analyzed by BNPAGE and in-gel NBT staining. Higher-molecular-weight bands were indicated by a red arrow. Fractions of 9–10 mL (elution volume) were used for negative staining EM and cryo-EM.

(C) Representative 2D class averages of different views show fine features of human $MCI_2III_2IV_2$ compared with the projections refined model. 1st and 3rd lines: 2D averaging results of 8.6 k particles used for the 3D auto-refinement process of $MCI_2III_2IV_2$. 2nd and 4th lines (in red rectangle line): projections of the $MCI_2III_2IV_2$ density map after auto-refinement.

(D) The 17.4 Å resolution $MCI_2III_2IV_2$ map with the sub-region refinement density maps of the $SCI_1III_2IV_1$ aligned. These maps are shown in three differently rotated views (left, side view along the inner membrane; right, top view from the matrix side; bottom, bottom view from the intermembrane side).

(E) The models of CI, CIII, and CIV were fitted into the sub-region refinement density maps already aligned to the $MCI_2III_2IV_2$ map. The structural models of CI, CIII, and CIV are colored in blue, brown, and magenta, respectively.

(F) The models of CI, CIII, CIV, and Cyt.*c* were docked into the density map of $MCI_2III_2IV_2$. The complexes and Cyt.*c* molecules are colored as labeled with texts in same colors, respectively.

See also Figures S1–S5 and Tables S1–S3.

model based solely on stoichiometry seems inaccurate in mammals, because the widely accepted plasticity model posits that not all CIIIs and CIVs are assembled into supercomplexes (Enríquez, 2016). In 2009, Kouril's group reported a megacomplex organization of I_2III_2 from potato mitochondria (Bultema et al., 2009). Particles larger than $SCI_1III_2IV_1$ were also detected in both BN-PAGE and cryo-EM images in that study.

In the present study, we report the highest resolution structure to date of human $SCI_1III_2IV_1$ and determine the circular architecture of megacomplex $I_2III_2IV_2$ ($MCI_2III_2IV_2$). Based on this structural information and previous functional analyses, we hypothesize that CII is also a part of the megacomplex. The structure of CII can be fitted into the megacomplex to form the electron transport chain supercomplex (ETCS), which contains all electron transport chain components. In the ETCS, CI and CII can use the same Q-pool sealed by CI, CII, CIII, and CIV, providing the most effective electron-transport pathways. Furthermore, inclusion of CII into the megacomplex can well explain the reverse electron transfer from succinate to NADH (Lenaz et al., 2016). Our structures represent the highest resolution structure to date of these huge human membrane supercomplexes. They reveal the precise arrangement of human respiratory chain complexes and further suggest that CI, CII, CIII, and CIV can function in a single mega-assembly. This information may facilitate the development of therapeutic applications for treating human diseases involving dysfunctional electron transport chain complexes.

RESULTS

Protein Purification and Structure Determination

The mitochondrial electron transport chain complexes are the major and most intricate components of the energy production system in cells (Acín-Pérez et al., 2008; Baradaran et al., 2013; Brandt, 2011; Bultema et al., 2009; Cogliati et al., 2013; Efremov et al., 2010; Fiedorczuk et al., 2016; Guo et al., 2016; Hunte et al., 2010; Iwata et al., 1998; Letts et al., 2016; Melber and Winge, 2016; Menezes et al., 2014; Rodenburg, 2016; Sánchez-Caballero et al., 2016; Schäfer et al., 2007; Schägger and Pfeiffer, 2000; Stroh et al., 2004; Tan et al., 2014; Tsukihara et al., 1995, 1996; Vinothkumar et al., 2014; Wu et al., 2016; Xia et al., 1997; Zhang et al., 1998; Zhu et al., 2016). We purified the human electron transport chain supercomplexes from HEK293 cells and obtained two major bands in the blue native gel with nitro blue tetrazolium staining (Figures 1A and 1B). The molecular weight of the lower band is ~1.7 MDa, which is consistent with $SCI_1III_2IV_1$, as previously described (Althoff et al., 2011; Gu et al., 2016; Letts et al., 2016; Sánchez-Caballero et al., 2016; Schäfer et al., 2007; Sousa et al., 2016; Wu et al., 2016). Using single-particle cryo-electron microscopy (cryo-EM) method and a combination of structure docking, homology building, and de novo modeling, we obtained the structures of human $SCI_1III_2IV_1$ and $MCI_2III_2IV_2$ at overall 3.9 and 17.4 Å, respectively (Figures 1C, S1 and S2; STAR Methods). The consistency between the 2D averaging results and the projections indicates that the 3D reconstruction model of $MCI_2III_2IV_2$ is reliable (Figure 1C).

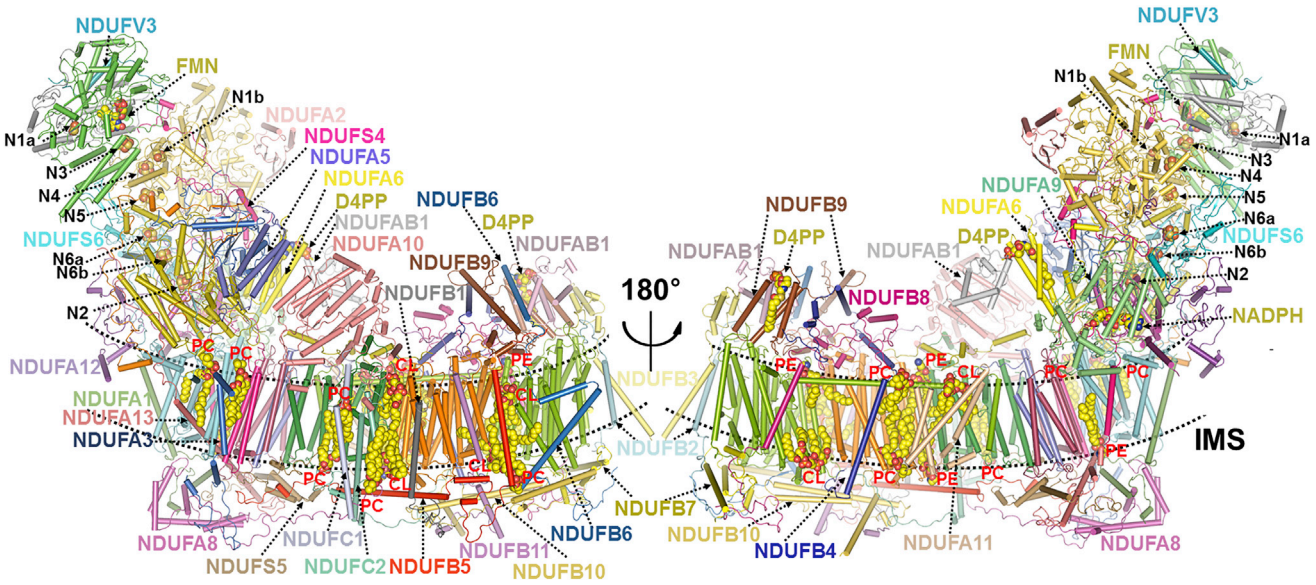

Figure 2. Overall Structure and Cofactors of Human CI

Cartoon representation of the human CI. Shown in two differently rotated views along the membrane. The transmembrane region is indicated by two dashed lines. IMS, intermembrane space. The cofactors are shown in spheres. PE, phosphatidylethanolamine; PC, phosphatidylcholine; CL, cardiolipin; D4PP, decanoyl (C10)-4′-phosphopantetheine.

See also Figures S1–S5 and Tables S1 and S3.

Sub-region refinement with different regions of $SCI_1III_2IV_1$ resulted in 3.4, 3.7, 3.7, 3.4, and 5.2 Å structures of the matrix arm of CI, membrane arm of CI, CI, CIII dimer, and CIV, respectively (Figure S3; STAR Methods). The well-resolved density maps allowed us to build the structure models into these maps in COOT (Emsley and Cowtan, 2004), with the majority of residues from all the subunits of CI and CIII (Figures S4A–S4C; Tables S1–S3). These sub-region structures were subsequently docked into the 3.9 Å density map of the $SCI_1III_2IV_1$ and further into the 17.4 Å $MCI_2III_2IV_2$ density map to obtain the complete structure (Figures 1D–1F and S5). The "gold standard" Fourier shell correlation (FSC) criterions between the models and maps have no dramatically differences, which indicate the models docking are accurate (Figure S4). In the final $MCI_2III_2IV_2$ structure, we could accurately place 14 core and 31 supernumerary subunits in each CI, 22 subunits in dimeric CIII, and do rigid body fitting of the 13 subunits in each CIV (PDB: 1OCC) (Tsukihara et al., 1996) and 2 cytochrome *c* (Cyt.*c*) molecules, as well as a multitude of cofactors (Figures 1E and 1F; Tables S1 and S2).

Structure of the Entire Human CI

Previous studies demonstrated that CI was the most complicated protein complex in mitochondria (Fiedorczuk et al., 2016; Rodenburg, 2016; Sánchez-Caballero et al., 2016; Stroud et al., 2016; Vinothkumar et al., 2014; Wirth et al., 2016; Zhu et al., 2016; Zickermann et al., 2015). It contains 45 protein subunits (44 different subunits), which bind many cofactors and are modified by numerous posttranslational modifications (Hornbeck et al., 2015). The 3.4, 3.7, and 3.7 Å of the matrix arm, membrane arm, and overall CI maps, respectively, allowed us to build all the 45 subunits and almost all of the residues with side chains into the human CI structure (Figures 2 and 3; Table S1). Among 8,499 residues of the mature human CI, 8,199 (96.47%) residues were modeled in our atomic structure of human CI and 8,159 (96.00%) residues were assigned with side chains (Table S1). All the residues of the 7 core subunits of the membrane arm have been assigned with side chains, although the sequence identity of these subunits only ranges from 58.29% to 77.67% (Table S1). For comparison, in the CI structures solved recently, the 4.2 Å resolution cryo-EM model of bovine CI only contained 27% residues of the supernumerary subunits with side chains (Zhu et al., 2016), and the 3.9 Å resolution cryo-EM model for the bovine CI structure contained 88% residues with side chains (Fiedorczuk et al., 2016). We also assigned an FMN molecule in NDUFV1, 8 FeS clusters for the electron transfer cascade in the matrix region, an NADPH molecule in NDUFA9, a Zn^{2+} ion in NDUFS6, and 2 phosphopantetheine molecules in both NDUFAB1a-NDUFA6 and NDUFAB1b-NDUFB9 complexes, respectively. Interestingly, the density also revealed 18 phospholipid molecules, which were involved in the protein-protein interactions in the membrane region, including 9 phosphatidylcholines (PCs), 4 phosphatidylethanolamines (PEs), and 5 cardiolipins (CLs) molecules (Figure 2).

As previously described, CI contains four functional modules, M_D, M_P, P_P, and P_D (Brandt, 2006, 2011; Hunte et al., 2010; Wirth et al., 2016; Wu et al., 2016). The matrix arm of CI contains M_D and M_P modules and protrudes out of the membrane by ~95 Å (Figure 3A). It is formed by 7 conserved core subunits with 8 FeS clusters and an FMN molecule surrounded by 10 supernumerary components. The membrane arm contains both P_P and P_D modules, which comprise four antiporter-like proton pumps

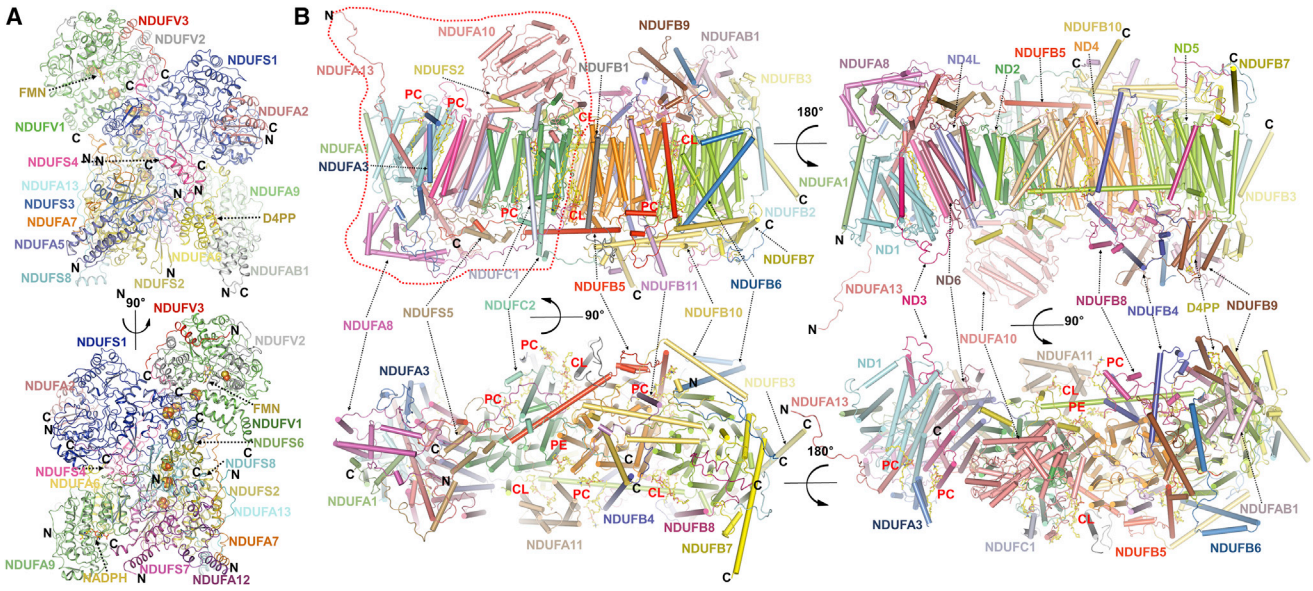

Figure 3. Structure Characters of Human CI

(A) The overall structure of the matrix arm of CI. Cartoon representation of the matrix arm in two differently rotated views. Seventeen subunits, including 7 core subunits (NDUFV1, NDUFV2, NDUFS1, NDUFS2, NDUFS3, NDUFS7, and NDUFS8) and 10 supernumerary subunits (NDUFV3, NDUFS4, NDUFS6, NDUFA2, NDUFA5, NDUFA6, NDUFA7, NDUFA9, NDUFA12, and NDUFAB1), are colored and labeled with text in the same colors, respectively. The FeS-clusters are shown in spheres. The FMN is shown in yellow sticks. D4PP, decanoyl (C10)-4′-phosphopantetheine.

(B) Cartoon representation of the membrane arm of human CI in four differently rotated views along the membrane. The subunits are colored and labeled with text in the same colors, respectively. The phospholipids are shown in yellow sticks and indicated in red text. The N and C termini are indicated. PE, phosphatidylethanolamine; PC, phosphatidylcholine; CL, cardiolipin; D4PP, decanoyl (C10)-4′-phosphopantetheine. The region in the red dash line is the P_P module.

See also Figures S1–S5 and Tables S1 and S3.

for proton translocation. The P_P module has two antiporter-like proton pumps, 5 core, and 9 supernumerary subunits. The P_D module has the other two antiporter-like proton pumps, 2 core, and 12 supernumerary subunits. The structural observations of the entire human CI structure are consistent with the previous conclusion that the widely linked supernumerary subunits interact extensively to form an integral complex (Fiedorczuk et al., 2016; Sánchez-Caballero et al., 2016; Wu et al., 2016; Zhu et al., 2016) (Figure 3B). The membrane arm of CI contains seven core subunits, 21 supernumerary subunits, and 18 phospholipid molecules. The phospholipid molecules participate in the protein-protein interactions and make the membrane arm of CI more flexible to perform its proton translocation activity (Figure 3B).

Cytochrome *c* Molecules Are in Loading-State to Accept Electrons

The structure of CIII has been extensively studied for two decades (Iwata et al., 1998; Xia et al., 1997; Zhang et al., 1998), but no human CIII has been resolved to date. In the present study, we solved the structure of human CIII at an overall resolution of 3.4 Å. The density map allowed us to build all 22 subunits and almost all residues into the human CIII dimeric structure. Interestingly, our maps showed that there were two globular densities on the surface of the CIII at the IMS side, which might belong to two partially attached Cyt.*c* molecules. We added two Cyt.*c* molecules into these densities with rigid body fitting (Figures 4A and S5). Among the 4,334 residues of the mature human CIII, we assigned a total of 4,218 (97.32%) residues with side chains (Table S2). We also assigned 3 PCs, 4 PEs, 7 CLs, 6 heme, and 2 [2Fe-2S] iron-sulfide molecules in the structure (Figure 4A). The overall structure of human CIII is similar to the structures of other CIIIs solved previously (Iwata et al., 1998; Solmaz and Hunte, 2008; Xia et al., 1997; Zhang et al., 1998).

Unlike the CIII in the intermediate state in the porcine SCI_1III_2-IV_1 (Sánchez-Caballero et al., 2016; Wu et al., 2016), the distances from both [2Fe-2S] iron-sulfide molecules of both UQCRFS1 subunits in the human CIII homodimer to heme b_L and c_1 are ~36 and 15 Å, respectively (Figure 4A). Interestingly, the binding sites of the Cyt.*c* molecules are different from those of Cyt.*c* in the reduced state (Solmaz and Hunte, 2008). In the yeast CIII structure containing reduced Cyt.*c*, the [2Fe-2S] iron-sulfide molecules in both UQCRFS1 subunits are close to the heme b_L (Solmaz and Hunte, 2008). In contrast, both UQCRFS1 subunits in human CIII move about 21 Å and are close to the heme c_1. The distance of two Cyt.*c* molecules in both structures is ~20 Å. As a result, the distance between the heme c_1 to the heme covalently bound to Cyt.*c* changes from ~17 to 27 Å (Figure 4B), which is too far to allow the electron transfer. These structural observations provide insight into the electron carrier [2Fe-2S] molecules that transfer electrons to the heme c_1 and loading-state of the Cyt.*c* molecules and further suggest the pathways of how Cyt.*c* binds and releases from CIII.

The conformational changes of both UQCRFS1 subunits of dimeric CIII not only indicate that both CIII monomers in the $MCI_2III_2IV_2$ are in the c_1 state (Iwata et al., 1998; Zhang et al.,

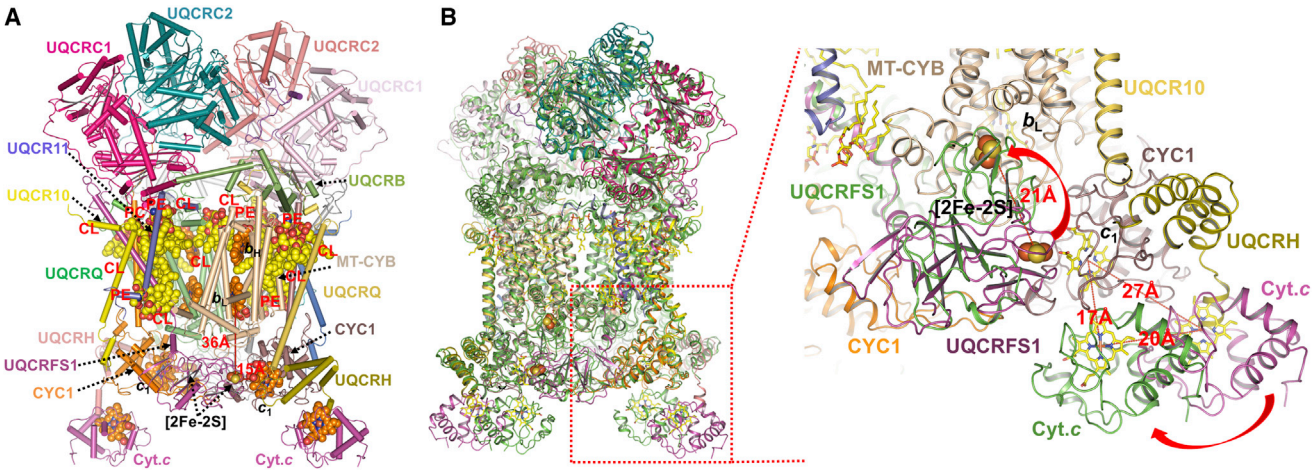

Figure 4. The Loading-State of Cyt.*c* in Human CIII

(A) Cartoon representation of the human CIII. Viewed along the membrane. The phospholipids and hemes are shown in yellow and orange spheres, respectively. The subunits and Cyt.*c* molecules are colored as labeled with text in the same colors, respectively.

(B) The loading-state Cyt.*c* of human CIII. Viewed along the membrane. Left: the human Cyt.*c* containing CIII model is aligned with the structure of the yeast CIII (PDB: 3CX5). The yeast CIII is colored in green. Right: the conformational changes of Cyt.*c*, [2Fe-2S] cluster and UQCRFS1 subunit. The phospholipid and heme molecules are shown in yellow sticks. The subunits are colored and labeled with text in the same colors, respectively.

See also Figures S1–S5 and Tables S2 and S3.

1998), but also suggest that both monomers in the CIII homodimer are active. The binding of two loading-state Cyt.*c* molecules in CIII further strengthens this conclusion. Our structural observation contradicts the previous suggestion that only one of the two electron transfer pathways in CIII homodimer is constitutively active, whereas the other is inactive (Sánchez-Caballero et al., 2016). It confirms our previous proposal that QH_2 (ubiquinol) released from CI could only diffuse to the Qi sites of CIII and could transfer two electrons to two Cyt.*c* at one time (Wu et al., 2016).

Disease-Related Mutations in CI and CIII

The mitochondrial electron transfer chain complexes are the major components of the energy production system in cells (Acín-Pérez et al., 2008; Baradaran et al., 2013; Brandt, 2011; Bultema et al., 2009; Cogliati et al., 2013; Efremov et al., 2010; Fiedorczuk et al., 2016; Gu et al., 2016; Guo et al., 2016; Hunte et al., 2010; Iwata et al., 1998; Letts et al., 2016; Melber and Winge, 2016; Menezes et al., 2014; Rodenburg, 2016; Schäfer et al., 2007; Schägger and Pfeiffer, 2000; Stroh et al., 2004; Tan et al., 2014; Tsukihara et al., 1995, 1996; Vinothkumar et al., 2014; Wu et al., 2016; Xia et al., 1997; Zhang et al., 1998; Zhu et al., 2016). Mutations in these proteins cause dysfunction of these complexes and are linked to different types of diseases (Table S4). The lack of structural information of human respiratory chain complexes seriously restricts our understanding of how these mutations influence the enzyme activity. In the present study, we solved the atomic resolution structures of human respiratory $SCI_1III_2IV_1$ and $MCI_2III_2IV_2$ with almost all residues assigned in CI and CIII (Tables S1 and S2). The structure showed that most of the mutations in the core subunits of CI and CIII reported in the literature, including those in NDUFV1, NDUFS1, ND1, ND5, and ND6 in CI and MT-CYB in CIII, target residues located at protein-protein interaction sites (Figure 5; Table S4). The supernumerary component NDUFS4 contains 11 identified mutations that are known to reduce the activity of CI (Table S4). Our structure shows that NDUFS4 extensively interacts with almost all components of the matrix arm in CI (Figure 3A), providing straightforward rationales for the detrimental effects of these mutations. The NDUFB4, NDUFB9, and NDUFA11 supernumerary subunits that are involved in the CI-CIII interactions (Wu et al., 2016) also contain several mutations, which are expected to decrease the stability of the protein complexes (Figure 5A; Table S4).

Structure of $MCI_2III_2IV_2$

The structure of human $MCI_2III_2IV_2$ has a similar architecture of the 2D-average of the supercomplex-I_2III_2 as previously described (Bultema et al., 2009). The $MCI_2III_2IV_2$ is ~220 Å in height, ~280 Å in width, and ~300 Å in length, and contains 140 subunits with 238 transmembrane helices (TMHs) (78 from CI, 13 TMHs from CIII, and 28 from CIV). All the TMHs are aligned in a slightly bent plane (Figure 6A). The dimeric CIII is in the center, with its 2-fold axis oriented perpendicularly to the membrane arms of the two surrounding CIs. Two CIVs are anchored by the distal end of the CI membrane arms and CIII dimer at each side, with a clear gap between CI and CIV (Figure 6B). This arrangement was most efficient, because both monomers of the CIII dimer could receive QH_2 from each CI and pass reduced Cyt.*c* to one adjacent CIV. This may be the ultimate oligomerization form of respiratory chain complexes functioning in emergency conditions.

Similar to the previously demonstrated porcine $SCI_1III_2IV_1$ structure (Wu et al., 2016), but symmetrically in this circular megacomplex, a loop of UQCRC1 of CIII inserted into the groove formed by the supernumerary subunits NDUFB9, NDUFAB1 of

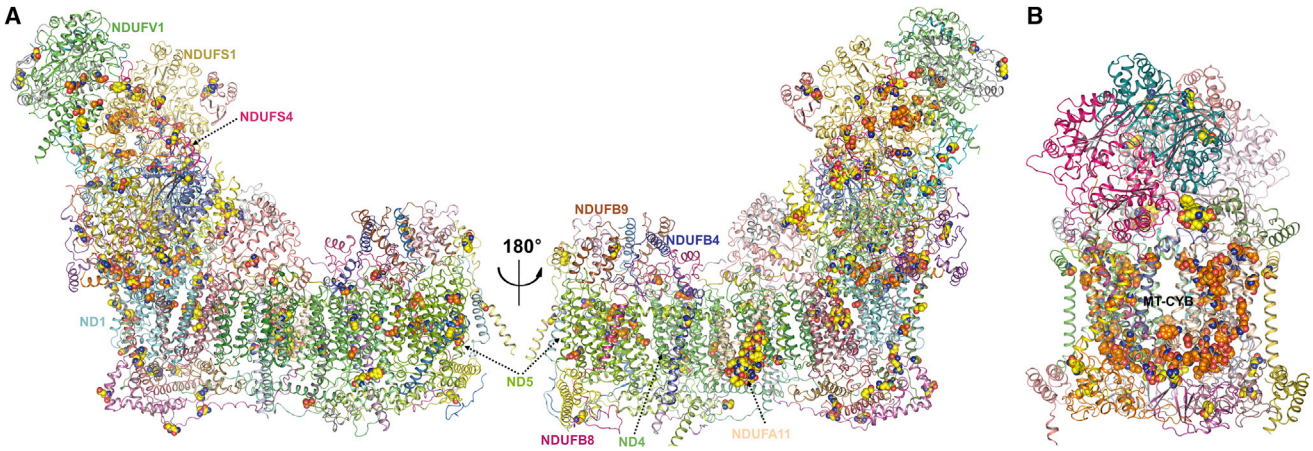

Figure 5. Disease-Related Mutations of Human CI and CIII

(A) Cartoon representation of the human CI in two differently rotated views along the membrane. The subunits are colored in different colors. The disease-related mutations are shown in spheres.

(B) Cartoon representation of the human CIII views along the membrane. The subunits are colored in different colors. The disease-related mutation residues are shown in spheres.

See also Tables S3 and S4.

CI, and the NDUFA11 of CI was close to the UQCRQ subunit of CIII. The COX7A subunit of each CIV was close to both CI and CIII (Figure S6). The interfaces between the CI-CIII and CI-CIV covered areas of 2,616 and 946 Å^2, respectively. There were no direct protein-protein interactions between CIII and CIV. Previous studies demonstrated that mitochondrial respiratory supercomplex formation was dependent on phospholipid molecules, especially cardiolipin molecules (Mileykovskaya and Dowhan, 2014). This suggests that the gaps between the complexes might be bridged by phospholipid molecules.

Model of ETCS

Structural analyses indicate that there is a large gap between CI and CIV (Figure 6B). We superposed the CIV dimer structure with Cyt.*c* (PDB: 5IY5) (Shimada et al., 2017) onto the CIV monomer of $MCI_2III_2IV_2$. The extra CIV clashed with both CI and CIII (Figure S7A), suggesting that the CIV in the supercomplex was a monomer. This structural observation is inconsistent with the previous model, assuming that the $SCI_1III_2IV_1$ could form a higher organization level through the dimerization of CIV (Letts et al., 2016). Previous studies suggested that the CII could interact with other mammalian electron transport chain complexes (CI, CIII, and CIV) in the megacomplexes (Acín-Pérez et al., 2008; Jiang et al., 2016; Lapuente-Brun et al., 2013; Schon and Dencher, 2009). Although we cannot locate the density of the CII in our map, previous protein-protein interaction studies demonstrated that the CII could interact with CI, CIII, and CIV (Floyd et al., 2016; Havugimana et al., 2012; Wan et al., 2015). The missing density might be due to the lower occupancy of CII in our protein samples. Alternatively, CII subunits were too dynamic and adopted multiple conformations, thus invisible due to data averaging. We modeled a porcine CII structure (Sun et al., 2005) into the gap, with the Q (ubiquinone)-binding site facing toward the CIII and the substrate succinate binding pocket facing the outside (Figures 7A–7C and S7B). The overall model contains all the complexes of electron transport chain components and is named ETCS (electron transport chain supercomplex) or $MCI_2II_2III_2IV_2$. In the ETCS, the SDHB subunit is close to the NDUFA9 supernumerary subunit of CI matrix, while the N-terminal loop of COX5A in CIV inserts into the groove formed by SDHA and SDHB (Figure 7B). Obviously, further investigations will be needed to verify this speculative model, especially structures with a higher resolution.

Based on this hypothesis, CI and CII can use the same Q-pool sealed by CI, CII, CIII, and CIV in the assembly (Figures 7C, S7C, and S7D). Although previous substrate channeling studies suggest that CI and CII use separate Q-pools (Lenaz et al., 2016), disputes about the segmentation of Q-pool still exist. Increasing evidence suggests that CI and CII use the same Q-pool in the inner mitochondrial membrane (Blaza et al., 2014; Milenkovic et al., 2017). We propose that, in emergency conditions, CII can join the $MCI_2III_2IV_2$ molecular machine to provide a most effective pathway to release the high-energy electrons. The distances of the Cyt.*c* pathways from the two reduced sites in CIII dimer are ~10 and ~11 nm, which indicates that the reduced Cyt.*c* molecules could diffuse to either CIV. Our structural observation of the two loading-state Cyt.*c* molecules implies that there might be a pathway between CIII and CIV to load and release the Cyt.*c* molecules (Figure 7D). In general, the Cyt.*c* is reduced by the heme c_1, diffuses to the CIV, transfers the electron to CIV, and reverts back to the oxidized state. When the [2Fe-2S] cluster of the UQCRFS1 subunit moves from the heme b_L to heme c_1, the conformational changes might induce the Cyt.*c* in the oxidized state to move from CIV back to CIII (Figure 6C). We termed this back-translocated Cyt.*c* as the loading-state Cyt.*c*.

DISCUSSION

Previous biochemical and structural biology studies (Acín-Pérez et al., 2008; Althoff et al., 2011; Bultema et al., 2009; Dudkina

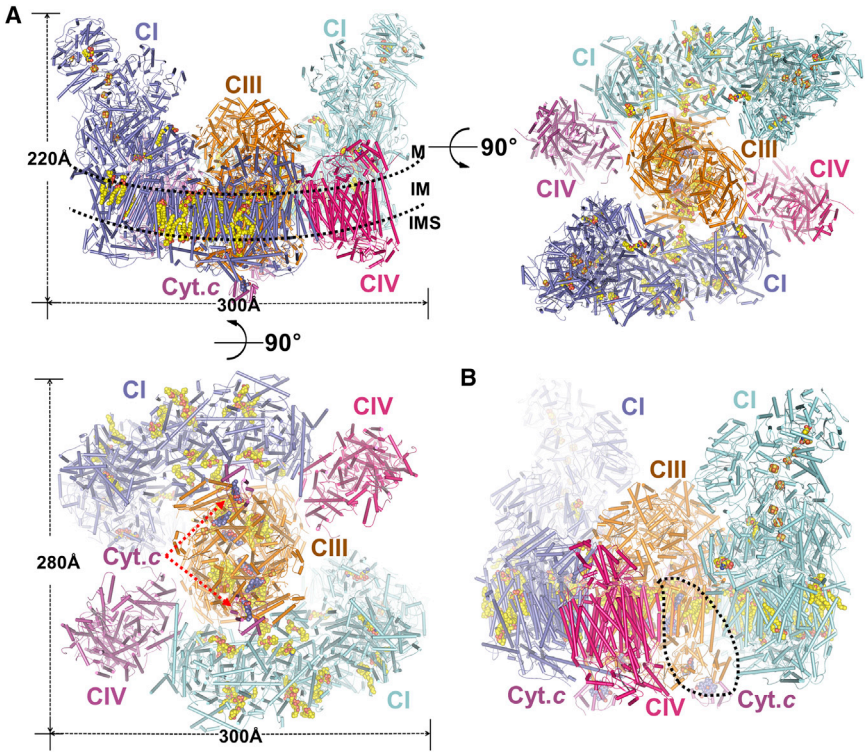

Figure 6. Structure of $MCI_2III_2IV_2$

(A) The overall structure of $MCI_2III_2IV_1$. The structure is shown in three differently rotated views (left, side view along the inner membrane; right, top view from the matrix side; bottom, bottom view from the intermembrane side). The transmembrane region is indicated by two dashed lines. M, matrix; IM, inner membrane; IMS, intermembrane space. The cofactors are shown in spheres. The complexes and Cyt.*c* molecules are colored as labeled with texts in the same colors, respectively.

(B) The gaps between CI and CIV in the $MCI_2III_2IV_1$. The gap was labeled with black dash line circle. The cofactors are shown in spheres. The complexes and Cyt.*c* molecules are colored as labeled with texts in the same colors, respectively.

See also Figures S6 and S7 and Table S1.

et al., 2011; Guo et al., 2016; Letts et al., 2016; Melber and Winge, 2016; Pérez-Pérez et al., 2016; Pfeiffer et al., 2003; Sánchez-Caballero et al., 2016; Schäfer et al., 2007; Sousa et al., 2016; Stroh et al., 2004; Wu et al., 2016) indicated that the CI, CIII, and CIV could assemble as a stable $SCI_1III_2IV_1$ and higher molecular weight megacomplexes. Increasing evidence now supports the plasticity model (Acín-Pérez et al., 2008; Enríquez, 2016) in which the respiratory chain complexes can assembly into supercomplexes to adapt to changing conditions through altering the quinary interactions (Cohen and Pielak, 2017). Although it has not been clearly established and remains controversial, formation of the supercomplexes might enhance the catalytic activity of individual components to enhance the efficiency of electron transfer through substrate channeling and to reduce the generation of reactive oxygen species (ROS) (Bakthavachalam and Shanmugam, 2017). The structures of the mammalian $SCI_1III_2IV_1$ from *Sus scrofa*, *Ovis aries*, and *Bos taurus* have been solved recently (Letts et al., 2016; Sánchez-Caballero et al., 2016; Sousa et al., 2016; Wu et al., 2016), but the organization and precise assignment of human respiratory chain complexes remain elusive. The biochemical functions of most of those human subunits remain to be fully characterized. Ultimately, high-resolution structures are required to better understand how disease-causing mutations affect the enzymatic activity or other functions of the respiratory chain complexes. In the present study, we used single-particle cryo-EM and sub-region refinement methods to obtain the near atomic resolution structure of human respiratory $SCI_1III_2IV_1$. Further data analyses indicate that the complexes could form a circular $MCI_2III_2IV_2$. More interestingly, the biological and structural analyses suggest that the CII could insert into the gap between CI and CIV in $MCI_2III_2IV_2$, which led us to propose a model of the ETCS ($MCI_2II_2III_2IV_2$). The architecture of ETCS suggests that all the electron transport chain complexes of the respiratory string could function as a single entity with high efficiency.

One of the most important questions of electron transport chain studies is how the redox energy (produced by electron transfers from the peripheral matrix arm of CI to the oxygen molecules in CIV) is harnessed to pump protons from the matrix side to the IMS. The molecular mechanism of how the electron transfer is coupled to the proton translocation in CI, CIII, and CIV has been studied for decades (Baradaran et al., 2013; Hunte et al., 2010; Iwata et al., 1998; Mitchell, 1975; Tsukihara et al., 1995, 1996; Xia et al., 1997; Zhang et al., 1998; Zickermann et al., 2015). The partial loading-state of the two Cyt.*c* proteins in the human $MCI_2III_2IV_2$ structure is consistent with the previous hypothesis that only the Q_i site could bind QH_2 and distribute two electrons to two Cyt.*c* in one cycle, while the protons from the QH_2 are translocated from the matrix to the IMS side (Wu et al., 2016).

Taking into consideration our previous findings with the porcine $SCI_1III_2IV_1$ structure (Wu et al., 2016), we propose a model to explain how the whole ETCS works (Figures 7C and 7D). The reduced electron carrier molecules NADH and succinate are generated by the Krebs cycle (tricarboxylic acid cycle) in the mitochondrial matrix and diffuse to the CI and CII, respectively. The electron transfer cascades from NADH to Q through the FeS clusters set up an electrical circuit for the CI machine to drive the translocation of four protons from the matrix side to the IMS side. QH_2 is released from the Q-chamber of CI and/or from the CII (that accept the electrons from the succinate to reduce Q to QH_2) to the Q-pool and diffuses to the Q_i binding site of CIII (Figures 7C, S7C, and S7D). The QH_2 in the Q_i site transfers two electrons to the b_H heme one by one and distributes them to two b_L hemes in both CIII homodimers, which could cause the conformational change of both UQCRFS1 subunits in CIII to allow the [2Fe-2S] clusters each to accept one

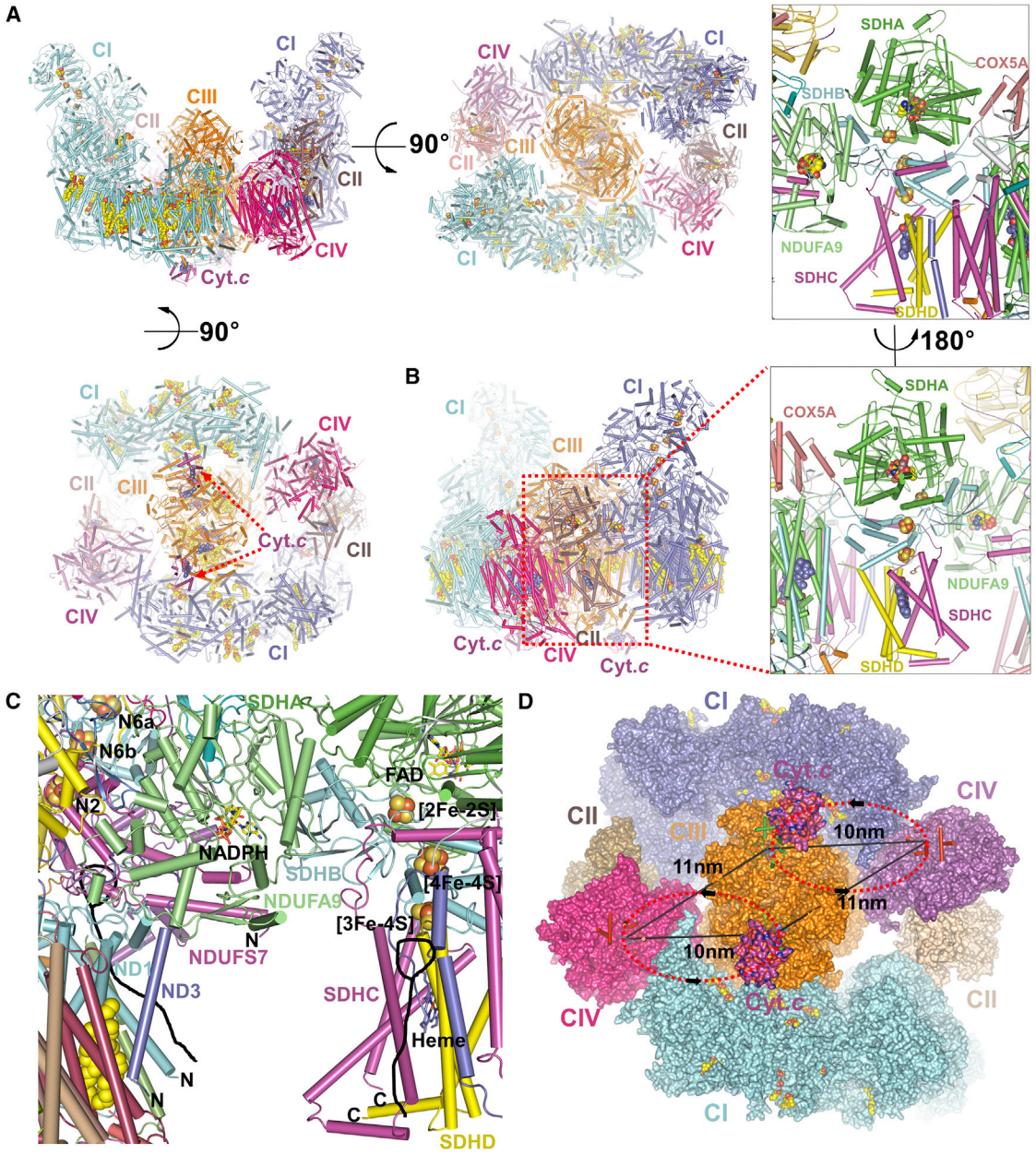

Figure 7. Model of ETCS

(A) Cartoon representation of the circular model of ETCS ($MCI_2II_2III_2IV_2$). This model is shown in three differently rotated views (left, side view along the inner membrane; right, top view from the matrix side; bottom, bottom view from the intermembrane side). The cofactors are shown in spheres. All the respiratory chain complexes and Cyt.*c* molecules are colored as labeled with texts in the same colors, respectively.

(B) The proposed interactions among CII, CI, and CIV in the ETCS. Shown in two differently rotated views alone the membrane. The cofactors are shown in spheres. The CII subunits and subunits participating in the interactions are colored as labeled with texts in the same colors, respectively.

(C) The ubiquinone-binding sites of CI and CII. The black stick models stand for ubiquinone molecules. The cofactors are shown in sticks. The Fe-S clusters and phospholipids are shown in spheres. The subunits of CI and CII are colored as labeled with texts in the same colors, respectively.

(D) The possible pathways of Cyt.*c* transfer in the ETCS model. Viewed from the intermembrane space side. All the respiratory chain complexes and loading-state Cyt.*c* molecules are shown in sphere and colored as labeled with texts in the same colors. Cyt.*c* molecules bounded in CIII and CIV are shown in cartoon and colored in green and red, respectively. The distances between these Cyt.*c* molecules are indicated. The two dash circular line indicate the pathways of the Cyt.*c*. See also Figure S7.

electron. Both UQCRFS1 subunits then change back to the c_1 state, wait for the two Cyt.*c* molecules to bind to the right positions (Figures 6C and 7D), and then transfer the two electrons to two Cyt.*c* molecules through the two c_1 hemes, respectively (Wu et al., 2016). Finally, both Cyt.*c* molecules with electrons are released from CIII and diffuse to CIVs at both sides through the Cyt.*c* diffusion pathways to transfer their electrons to CIV. The O_2 is reduced to H_2O, accompanied by the translocation of two protons (Figure 7D).

In summary, our structures of human $SCI_1III_2IV_1$ and $MCI_2III_2IV_2$ provide a wealth of high-resolution structural information about the human CI and CIII. The proposed model of ETCS suggests a feasible spatial arrangement of the electron transport chain complexes. Our results rationalize the detrimental effects of disease-causing mutations in the human CI and CIII and provide a framework for future in-depth mechanistic studies of the respiratory string.

STAR★METHODS

Detailed methods are provided in the online version of this paper and include the following:

- KEY RESOURCES TABLE
- CONTACT FOR REAGENT AND RESOURCE SHARING
- EXPERIMENTAL MODEL AND SUBJECT DETAILS
  - Cell Culture
- METHOD DETAILS
  - Mitochondria Preparation
  - Human Electron Transport Chain Supercomplexes Purification
  - Blue Native PAGE
  - NBT Staining
  - Cryo-EM Data Acquisition and Processing
  - Image Processing
  - Model Building and Refinement
- QUANTIFICATION AND STATISTICAL ANALYSIS
- DATA AND SOFTWARE AVAILABILITY

SUPPLEMENTAL INFORMATION

Supplemental Information includes seven figures and four tables and can be found with this article online at http://dx.doi.org/10.1016/j.cell.2017.07.050.

AUTHOR CONTRIBUTIONS

M.Y. conceived, designed, and supervised the project, built the model, analyzed the data, and wrote the manuscript. J.G., S.Z., and R.G. did the protein purification and detergent screening. M.W. performed EM sample preparation, data collection, and structural determination. All authors discussed the data of the manuscript.

ACKNOWLEDGMENTS

We thank the Tsinghua University Branch of China National Center for Protein Sciences (Beijing) for providing the facility support. The computation was completed on the "Explorer 100" cluster system of Tsinghua National Laboratory for Information Science and Technology. This work was supported by funds from the National Key R&D Program of China (2017YFA0504600 and 2016YFA0501100), the National Science Fund for Distinguished Young Scholars (31625008), and the National Natural Science Foundation of China (21532004 and 31570733).

Received: May 11, 2017
Revised: June 20, 2017
Accepted: July 28, 2017
Published: August 24, 2017

REFERENCES

Acín-Pérez, R., Fernández-Silva, P., Peleato, M.L., Pérez-Martos, A., and Enriquez, J.A. (2008). Respiratory active mitochondrial supercomplexes. Mol. Cell *32*, 529–539.

Adams, P.D., Afonine, P.V., Bunkóczi, G., Chen, V.B., Davis, I.W., Echols, N., Headd, J.J., Hung, L.W., Kapral, G.J., Grosse-Kunstleve, R.W., et al. (2010). PHENIX: a comprehensive Python-based system for macromolecular structure solution. Acta Crystallogr. D Biol. Crystallogr. *66*, 213–221.

Althoff, T., Mills, D.J., Popot, J.L., and Kühlbrandt, W. (2011). Arrangement of electron transport chain components in bovine mitochondrial supercomplex I1III2IV1. EMBO J. *30*, 4652–4664.

Bakthavachalam, P., and Shanmugam, P.S. (2017). Mitochondrial dysfunction - silent killer in cerebral ischemia. J. Neurol. Sci. *375*, 417–423.

Baradaran, R., Berrisford, J.M., Minhas, G.S., and Sazanov, L.A. (2013). Crystal structure of the entire respiratory complex I. Nature *494*, 443–448.

Berrisford, J.M., and Sazanov, L.A. (2009). Structural basis for the mechanism of respiratory complex I. J. Biol. Chem. *284*, 29773–29783.

Blaza, J.N., Serreli, R., Jones, A.J., Mohammed, K., and Hirst, J. (2014). Kinetic evidence against partitioning of the ubiquinone pool and the catalytic relevance of respiratory-chain supercomplexes. Proc. Natl. Acad. Sci. USA *111*, 15735–15740.

Brandt, U. (2006). Energy converting NADH:quinone oxidoreductase (complex I). Annu. Rev. Biochem. *75*, 69–92.

Brandt, U. (2011). A two-state stabilization-change mechanism for proton-pumping complex I. Biochim. Biophys. Acta *1807*, 1364–1369.

Bultema, J.B., Braun, H.P., Boekema, E.J., and Kouril, R. (2009). Megacomplex organization of the oxidative phosphorylation system by structural analysis of respiratory supercomplexes from potato. Biochim. Biophys. Acta *1787*, 60–67.

Chen, S., McMullan, G., Faruqi, A.R., Murshudov, G.N., Short, J.M., Scheres, S.H., and Henderson, R. (2013). High-resolution noise substitution to measure overfitting and validate resolution in 3D structure determination by single particle electron cryomicroscopy. Ultramicroscopy *135*, 24–35.

Cogliati, S., Frezza, C., Soriano, M.E., Varanita, T., Quintana-Cabrera, R., Corrado, M., Cipolat, S., Costa, V., Casarin, A., Gomes, L.C., et al. (2013). Mitochondrial cristae shape determines respiratory chain supercomplexes assembly and respiratory efficiency. Cell *155*, 160–171.

Cohen, R.D., and Pielak, G.J. (2017). A cell is more than the sum of its (dilute) parts: A brief history of quinary structure. Protein Sci. *26*, 403–413.

Dudkina, N.V., Kudryashev, M., Stahlberg, H., and Boekema, E.J. (2011). Interaction of complexes I, III, and IV within the bovine respirasome by single particle cryoelectron tomography. Proc. Natl. Acad. Sci. USA *108*, 15196–15200.

Efremov, R.G., Baradaran, R., and Sazanov, L.A. (2010). The architecture of respiratory complex I. Nature *465*, 441–445.

Emsley, P., and Cowtan, K. (2004). Coot: model-building tools for molecular graphics. Acta Crystallogr. D Biol. Crystallogr. *60*, 2126–2132.

Emsley, P., Lohkamp, B., Scott, W.G., and Cowtan, K. (2010). Features and development of Coot. Acta Crystallogr. D Biol. Crystallogr. *66*, 486–501.

Enríquez, J.A. (2016). Supramolecular organization of respiratory complexes. Annu. Rev. Physiol. *78*, 533–561.

Fernández-Vizarra, E., and Zeviani, M. (2015). Nuclear gene mutations as the cause of mitochondrial complex III deficiency. Front. Genet. *6*, 134.

Fiedorczuk, K., Letts, J.A., Degliesposti, G., Kaszuba, K., Skehel, M., and Sazanov, L.A. (2016). Atomic structure of the entire mammalian mitochondrial complex I. Nature *538*, 406–410.

Floyd, B.J., Wilkerson, E.M., Veling, M.T., Minogue, C.E., Xia, C., Beebe, E.T., Wrobel, R.L., Cho, H., Kremer, L.S., Alston, C.L., et al. (2016). Mitochondrial protein interaction mapping identifies regulators of respiratory chain function. Mol. Cell *63*, 621–632.

Gu, J., Wu, M., Guo, R., Yan, K., Lei, J., Gao, N., and Yang, M. (2016). The architecture of the mammalian respirasome. Nature *537*, 639–643.

Guo, R., Gu, J., Wu, M., and Yang, M. (2016). Amazing structure of respirasome: unveiling the secrets of cell respiration. Protein Cell *7*, 854–865.

Havugimana, P.C., Hart, G.T., Nepusz, T., Yang, H., Turinsky, A.L., Li, Z., Wang, P.I., Boutz, D.R., Fong, V., Phanse, S., et al. (2012). A census of human soluble protein complexes. Cell *150*, 1068–1081.

Heinemeyer, J., Braun, H.P., Boekema, E.J., and Kouril, R. (2007). A structural model of the cytochrome C reductase/oxidase supercomplex from yeast mitochondria. J. Biol. Chem. *282*, 12240–12248.

Hornbeck, P.V., Zhang, B., Murray, B., Kornhauser, J.M., Latham, V., and Skrzypek, E. (2015). PhosphoSitePlus, 2014: mutations, PTMs and recalibrations. Nucleic Acids Res. *43*, D512–D520.

Hunte, C., Zickermann, V., and Brandt, U. (2010). Functional modules and structural basis of conformational coupling in mitochondrial complex I. Science *329*, 448–451.

Iwata, S., Lee, J.W., Okada, K., Lee, J.K., Iwata, M., Rasmussen, B., Link, T.A., Ramaswamy, S., and Jap, B.K. (1998). Complete structure of the 11-subunit bovine mitochondrial cytochrome bc1 complex. Science *281*, 64–71.

Jiang, X., Li, L., Ying, Z., Pan, C., Huang, S., Li, L., Dai, M., Yan, B., Li, M., Jiang, H., et al. (2016). A Small molecule that protects the integrity of the electron transfer chain blocks the mitochondrial apoptotic pathway. Mol. Cell *63*, 229–239.

Kucukelbir, A., Sigworth, F.J., and Tagare, H.D. (2014). Quantifying the local resolution of cryo-EM density maps. Nat. Methods *11*, 63–65.

Kuonen, D.R., Roberts, P.J., and Cottingham, I.R. (1986). Purification and analysis of mitochondrial membrane proteins on nondenaturing gradient polyacrylamide gels. Anal. Biochem. *153*, 221–226.

Lapuente-Brun, E., Moreno-Loshuertos, R., Acín-Pérez, R., Latorre-Pellicer, A., Colás, C., Balsa, E., Perales-Clemente, E., Quirós, P.M., Calvo, E., Rodríguez-Hernández, M.A., et al. (2013). Supercomplex assembly determines electron flux in the mitochondrial electron transport chain. Science *340*, 1567–1570.

Lenaz, G., Tioli, G., Falasca, A.I., and Genova, M.L. (2016). Complex I function in mitochondrial supercomplexes. Biochim. Biophys. Acta *1857*, 991–1000.

Letts, J.A., Fiedorczuk, K., and Sazanov, L.A. (2016). The architecture of respiratory supercomplexes. Nature *537*, 644–648.

Li, X., Mooney, P., Zheng, S., Booth, C.R., Braunfeld, M.B., Gubbens, S., Agard, D.A., and Cheng, Y. (2013). Electron counting and beam-induced motion correction enable near-atomic-resolution single-particle cryo-EM. Nat. Methods *10*, 584–590.

Melber, A., and Winge, D.R. (2016). Inner secrets of the respirasome. Cell *167*, 1450–1452.

Menezes, M.J., Riley, L.G., and Christodoulou, J. (2014). Mitochondrial respiratory chain disorders in childhood: insights into diagnosis and management in the new era of genomic medicine. Biochim. Biophys. Acta *1840*, 1368–1379.

Milenkovic, D., Blaza, J.N., Larsson, N.G., and Hirst, J. (2017). The enigma of the respiratory chain supercomplex. Cell Metab. *25*, 765–776.

Mileykovskaya, E., and Dowhan, W. (2014). Cardiolipin-dependent formation of mitochondrial respiratory supercomplexes. Chem. Phys. Lipids *179*, 42–48.

Mindell, J.A., and Grigorieff, N. (2003). Accurate determination of local defocus and specimen tilt in electron microscopy. J. Struct. Biol. *142*, 334–347.

Mitchell, P. (1975). The protonmotive Q cycle: a general formulation. FEBS Lett. *59*, 137–139.

Moriarty, N.W., Grosse-Kunstleve, R.W., and Adams, P.D. (2009). electronic Ligand Builder and Optimization Workbench (eLBOW): a tool for ligand coordinate and restraint generation. Acta Crystallogr. D Biol. Crystallogr. *65*, 1074–1080.

Pérez-Pérez, R., Lobo-Jarne, T., Milenkovic, D., Mourier, A., Bratic, A., García-Bartolomé, A., Fernández-Vizarra, E., Cadenas, S., Delmiro, A., García-Consuegra, I., et al. (2016). COX7A2L is a mitochondrial complex III binding protein that stabilizes the III2+IV supercomplex without affecting respirasome formation. Cell Rep. *16*, 2387–2398.

Pettersen, E.F., Goddard, T.D., Huang, C.C., Couch, G.S., Greenblatt, D.M., Meng, E.C., and Ferrin, T.E. (2004). UCSF Chimera–a visualization system for exploratory research and analysis. J. Comput. Chem. *25*, 1605–1612.

Pfeiffer, K., Gohil, V., Stuart, R.A., Hunte, C., Brandt, U., Greenberg, M.L., and Schägger, H. (2003). Cardiolipin stabilizes respiratory chain supercomplexes. J. Biol. Chem. *278*, 52873–52880.

Rak, M., Bénit, P., Chrétien, D., Bouchereau, J., Schiff, M., El-Khoury, R., Tzagoloff, A., and Rustin, P. (2016). Mitochondrial cytochrome c oxidase deficiency. Clin. Sci. *130*, 393–407.

Rodenburg, R.J. (2016). Mitochondrial complex I-linked disease. Biochim. Biophys. Acta *1857*, 938–945.

Sánchez-Caballero, L., Guerrero-Castillo, S., and Nijtmans, L. (2016). Unraveling the complexity of mitochondrial complex I assembly: A dynamic process. Biochim. Biophys. Acta *1857*, 980–990.

Schäfer, E., Dencher, N.A., Vonck, J., and Parcej, D.N. (2007). Three-dimensional structure of the respiratory chain supercomplex I1III2IV1 from bovine heart mitochondria. Biochemistry *46*, 12579–12585.

Schägger, H., and Pfeiffer, K. (2000). Supercomplexes in the respiratory chains of yeast and mammalian mitochondria. EMBO J. *19*, 1777–1783.

Scheres, S.H. (2012). RELION: implementation of a Bayesian approach to cryo-EM structure determination. J. Struct. Biol. *180*, 519–530.

Scheres, S.H., and Chen, S. (2012). Prevention of overfitting in cryo-EM structure determination. Nat. Methods *9*, 853–854.

Schon, E.A., and Dencher, N.A. (2009). Heavy breathing: energy conversion by mitochondrial respiratory supercomplexes. Cell Metab. *9*, 1–3.

Shimada, S., Shinzawa-Itoh, K., Baba, J., Aoe, S., Shimada, A., Yamashita, E., Kang, J., Tateno, M., Yoshikawa, S., and Tsukihara, T. (2017). Complex structure of cytochrome c-cytochrome c oxidase reveals a novel protein-protein interaction mode. EMBO J. *36*, 291–300.

Shinzawa-Itoh, K., Shimomura, H., Yanagisawa, S., Shimada, S., Takahashi, R., Oosaki, M., Ogura, T., and Tsukihara, T. (2016). Purification of active respiratory supercomplex from bovine heart mitochondria enables functional studies. J. Biol. Chem. *291*, 4178–4184.

Solmaz, S.R., and Hunte, C. (2008). Structure of complex III with bound cytochrome c in reduced state and definition of a minimal core interface for electron transfer. J. Biol. Chem. *283*, 17542–17549.

Sousa, P.M., Videira, M.A., Santos, F.A., Hood, B.L., Conrads, T.P., and Melo, A.M. (2013). The bc:caa3 supercomplexes from the Gram positive bacterium Bacillus subtilis respiratory chain: a megacomplex organization? Arch. Biochem. Biophys. *537*, 153–160.

Sousa, J.S., Mills, D.J., Vonck, J., and Kühlbrandt, W. (2016). Functional asymmetry and electron flow in the bovine respirasome. eLife *5*. http://dx.doi.org/10.7554/eLife.21290.

Stroh, A., Anderka, O., Pfeiffer, K., Yagi, T., Finel, M., Ludwig, B., and Schägger, H. (2004). Assembly of respiratory complexes I, III, and IV into NADH oxidase supercomplex stabilizes complex I in Paracoccus denitrificans. J. Biol. Chem. *279*, 5000–5007.

Stroud, D.A., Surgenor, E.E., Formosa, L.E., Reljic, B., Frazier, A.E., Dibley, M.G., Osellame, L.D., Stait, T., Beilharz, T.H., Thorburn, D.R., et al. (2016). Accessory subunits are integral for assembly and function of human mitochondrial complex I. Nature *538*, 123–126.

Sun, F., Huo, X., Zhai, Y., Wang, A., Xu, J., Su, D., Bartlam, M., and Rao, Z. (2005). Crystal structure of mitochondrial respiratory membrane protein complex II. Cell *121*, 1043–1057.

Tan, A.S., Baty, J.W., and Berridge, M.V. (2014). The role of mitochondrial electron transport in tumorigenesis and metastasis. Biochim. Biophys. Acta *1840*, 1454–1463.

Tang, G., Peng, L., Baldwin, P.R., Mann, D.S., Jiang, W., Rees, I., and Ludtke, S.J. (2007). EMAN2: an extensible image processing suite for electron microscopy. J. Struct. Biol. *157*, 38–46.

Tsukihara, T., Aoyama, H., Yamashita, E., Tomizaki, T., Yamaguchi, H., Shinzawa-Itoh, K., Nakashima, R., Yaono, R., and Yoshikawa, S. (1995). Structures of metal sites of oxidized bovine heart cytochrome c oxidase at 2.8 A. Science *269*, 1069–1074.

Tsukihara, T., Aoyama, H., Yamashita, E., Tomizaki, T., Yamaguchi, H., Shinzawa-Itoh, K., Nakashima, R., Yaono, R., and Yoshikawa, S. (1996). The whole structure of the 13-subunit oxidized cytochrome c oxidase at 2.8 A. Science *272*, 1136–1144.

Vinothkumar, K.R., Zhu, J., and Hirst, J. (2014). Architecture of mammalian respiratory complex I. Nature *515*, 80–84.

Wan, C., Borgeson, B., Phanse, S., Tu, F., Drew, K., Clark, G., Xiong, X., Kagan, O., Kwan, J., Bezginov, A., et al. (2015). Panorama of ancient metazoan macromolecular complexes. Nature *525*, 339–344.

Wirth, C., Brandt, U., Hunte, C., and Zickermann, V. (2016). Structure and function of mitochondrial complex I. Biochim. Biophys. Acta *1857*, 902–914.

Wittig, I., Braun, H.P., and Schägger, H. (2006a). Blue native PAGE. Nat. Protoc. *1*, 418–428.

Wittig, I., Carrozzo, R., Santorelli, F.M., and Schägger, H. (2006b). Supercomplexes and subcomplexes of mitochondrial oxidative phosphorylation. Biochim. Biophys. Acta *1757*, 1066–1072.

Wu, M., Gu, J., Guo, R., Huang, Y., and Yang, M. (2016). Structure of mammalian respiratory supercomplex I1III2IV1. Cell *167*, 1598–1609.

Xia, D., Yu, C.A., Kim, H., Xia, J.Z., Kachurin, A.M., Zhang, L., Yu, L., and Deisenhofer, J. (1997). Crystal structure of the cytochrome bc1 complex from bovine heart mitochondria. Science *277*, 60–66.

Zhang, Z., Huang, L., Shulmeister, V.M., Chi, Y.I., Kim, K.K., Hung, L.W., Crofts, A.R., Berry, E.A., and Kim, S.H. (1998). Electron transfer by domain movement in cytochrome bc1. Nature *392*, 677–684.

Zheng, S.Q., Palovcak, E., Armache, J.P., Verba, K.A., Cheng, Y., and Agard, D.A. (2017). MotionCor2: anisotropic correction of beam-induced motion for improved cryo-electron microscopy. Nat. Methods *14*, 331–332.

Zhu, J., Vinothkumar, K.R., and Hirst, J. (2016). Structure of mammalian respiratory complex I. Nature *536*, 354–358.

Zickermann, V., Wirth, C., Nasiri, H., Siegmund, K., Schwalbe, H., Hunte, C., and Brandt, U. (2015). Structural biology. Mechanistic insight from the crystal structure of mitochondrial complex I. Science *347*, 44–49.

STAR★METHODS

KEY RESOURCES TABLE

REAGENT or RESOURCE	SOURCE	IDENTIFIER
Chemicals, Peptides, and Recombinant Proteins		
Trizma base	Sigma	T4661; CAS: 77-86-1
D-Sorbitol	Sigma	S1876; CAS: 50-70-4
KCl	Sigma	746436; CAS: 7447-40-7
EGTA	Sigma	E4378; CAS: 67-42-5
BSA	AMRESCO	0332; CAS: 9048-46-8
Percoll	GE Healthcare	17-0891-09
Digitonin	Sigma	D141; CAS: 11024-24-1
Glycine	Sigma	G7126; CAS: 56-40-6
4-Nitro blue tetrazolium chloride (NBT)	Sigma	N6876; CAS: 298-83-9
β-Nicotinamide adenine dinucleotide, reduced (β-NADH)	Sigma	N8129; CAS: 606-68-8 (Anhydrous)
6-Aminohexanoic acid	Sigma	07260; CAS: 60-32-2
Coomassie brilliant blue G-250	AMRESCO	0615; CAS: 6104-58-1
Glycerol	Sigma	G6279; CAS: 56-81-5
Ponceau S	Sigma	P3504; CAS: 6226-79-5
Acrylamide	Vetec	V900845; CAS: 79-06-1
N,N′-Methylenebis(acrylamide)	Vetec	V900301; CAS: 110-26-9
Tricine	Sigma	T0377; CAS: 5704-04-1
Imidazole	Sigma	I202; CAS: 288-32-4
Ammonium persulfate	Sigma	A3678; CAS: 7727-54-0
TEMED	Sigma	T22500; CAS: 110-18-9
SMM 293-TI medium	Sino Biological	Cat#M293TI
Penicillin/Streptomycin	Solarbio	Cat#P1400
Deposited Data		
Coordinates of matrix arm of the human CI	This study	PDB: 5XTB
Coordinates of membrane arm of the human CI	This study	PDB: 5XTC
Coordinates of the human CI	This study	PDB: 5XTD
Coordinates of the human CIII	This study	PDB: 5XTE
Coordinates of the human $SCI_1III_2IV_1$	This study	PDB: 5XTH
Coordinates of the human $MCI_2III_2IV_2$	This study	PDB: 5XTI
Cryo-EM map of matrix arm of the human CI	This study	EMDB: EMD-6771
Cryo-EM map of membrane arm of the human CI	This study	EMDB: EMD-6772
Cryo-EM map of the human CI	This study	EMDB: EMD-6773
Cryo-EM map of the human CIII	This study	EMDB: EMD-6774
Cryo-EM map of the human $SCI_1III_2IV_1$	This study	EMDB: EMD-6775
Cryo-EM map of the human $MCI_2III_2IV_2$	This study	EMDB: EMD-6776
Coordinates of bovine heart CIV	Tsukihara et al., 1996	PDB: 1OCC
Coordinates of cytochrome *c*-CIV complex	Shimada et al., 2017	PDB: 5IY5
Coordinates of yeast cytochrome *c*-CIII complex	Solmaz and Hunte, 2008	PDB: 3CX5
Coordinates of porcine $SCI_1III_2IV_1$	Wu et al., 2016	PDB: 5GUP
Experimental Models: Cell Lines		
Freestyle 293-F cells	Invitrogen	Cat#R790-07
Software and Algorithms		
AutoEMation2	written by Jianlin Lei (jllei@tsinghua.edu.cn)	N/A

(*Continued on next page*)

Continued

REAGENT or RESOURCE	SOURCE	IDENTIFIER
EMAN2.1	Tang et al., 2007	http://blake.bcm.edu/emanwiki/EMAN2
RELION1.4	Scheres, 2012	http://www2.mrc-lmb.cam.ac.uk/relion/index.php/Main_Page
CTFFIND3	Mindell and Grigorieff, 2003	http://grigoriefflab.janelia.org/ctf
ResMap	Kucukelbir et al., 2014	http://resmap.sourceforge.net/
COOT	Emsley et al., 2010	http://www2.mrc-lmb.cam.ac.uk/Personal/pemsley/coot
PHENIX	Adams et al., 2010	https://www.phenix-online.org/
UCSF Chimera	Pettersen et al., 2004	http://www.cgl.ucsf.edu/chimera
MotionCorr	Li et al., 2013	http://cryoem.ucsf.edu/software/driftcorr.html
MotionCor2	Zheng et al., 2017	http://msg.ucsf.edu/em/software/motioncor2.html
PyMOL	PyMOL	http://www.pymol.org

CONTACT FOR REAGENT AND RESOURCE SHARING

For reagents in this paper or more information about resource sharing, please contact the Lead Contact Maojun Yang (maojunyang@tsinghua.edu.cn).

EXPERIMENTAL MODEL AND SUBJECT DETAILS

Cell Culture

HEK293F cells were cultured in SMM 293-TI medium (Sino Biological) supplemented with 1 × penicillin/streptomycin (Solarbio) at 37°C with 8% CO_2.

METHOD DETAILS

Mitochondria Preparation

All procedures are carried out at 4°C. Four liters HEK293F cells were harvested before cell density reached 2.0 × 10^6 cells/mL and suspended by buffer-A (100 mM Tris pH 7.4, 225 mM sorbitol, 60 mM KCl, 1 mM EGTA and 0.1% BSA). The suspension was homogenized by a soft blender for 150 s and the homogenate was centrifuged at 3,000 × *g* for 10 min. Supernatant was further centrifuged at 20,000 × *g* for 30 min to obtain the crude mitochondria. The pellet was suspended in buffer-B (100 mM Tris pH 7.4, 250 mM sucrose, 60 mM KCl, 40% Percoll and 0.1 mM EGTA) and centrifuged at 60,000 × *g* for 50 min. The clear mitochondria layer was extracted carefully and diluted with buffer-C (100 mM Tris pH7.4, 100 mM Sorbitol, 60 mM KCl, 0.05 mM EGTA). The highly pure mitochondria were collected by centrifugation for 30 min at 20,000 × *g*.

Human Electron Transport Chain Supercomplexes Purification

Pure mitochondria were extracted by 1% (w/v) digitonin overnight with slow stirring at 4 °C in buffer-C. The extraction was centrifuged at 150,000 × *g* for 30 min at 4°C and the supernatant was concentrated to 1 mL by 100 kDa cutoff centrifugal filter (Millipore). Concentrated sample was loaded and centrifuged on 0.6-1.8 M sucrose gradients in buffer-D (25 mM Tris, pH 7.4, 60 mM KCl, 0.1% digitonin) at 150,000 × *g* for 20 hr at 4°C with a SW41 rotor (Beckman). Gradients were fractionated and investigated by 3%–10% BN-PAGE (Blue native PAGE). The supercomplexes were concentrated and finally purified by Superose 6 10/300 GL column (GE Healthcare) in buffer-E (10 mM Tris pH 7.4, 60 mM KCl and 0.1% digitonin). The peak fractions were collected for EM sample preparation, the purity of $SCI_1III_2IV_1$ and $MCI_2III_2IV_2$ was verified by BN-PAGE and NBT (Nitro blue tetrazolium) staining.

Blue Native PAGE

Blue native PAGE technique was used to determine native respiratory supercomplexes masses. The maker in this paper was generated by digitonin-solubilized mitochondria added with 10 × loading buffer (500 mM 6-aminohexanoic acid, 5% (w/v) Coomassie brilliant blue G-250, 50% (w/v) glycerol). Chromatographically purified respiratory supercomplexes or megacomplexes protein samples were mixed with 10 × loading buffer (0.1% (w/v) Ponceau S, 50% (w/v) glycerol) and subjected to 3%–10% blue native PAGE mini gel (1.5 × 8.3 × 7.3mm) for electrophoresis at 4 °C. After the native gel electrophoresis was conducted at 150 V for 30 min, cathode

buffer B (50 mM Tricine, 7.5 mM imidazole, 0.02% Coomassie brilliant blue G-250) was changed to cathode buffer B/10 (50 mM Tricine, 7.5 mM imidazole, 0.002% Coomassie brilliant blue G-250) and the running continued at 150 V for about 3 hr. All these buffers and procedures above were based on the Blue native PAGE Nature protocol (Wittig et al., 2006a).

NBT Staining

Nitro blue tetrazolium (NBT) is a soluble yellow chemical compound which has two tetrazole moieties. NBT will form blue or purple precipitate formazan, when it is reduced. NBT staining is used for specific in-gel activity assays of NADH dehydrogenase. For NBT staining, BN-PAGE gels were incubated in buffer containing 100 mM Tris-glycine pH 7.4, 1 mg/ml NBT and 100 mM β-NADH for 5-10 min (Kuonen et al., 1986).

Cryo-EM Data Acquisition and Processing

4 μL aliquots of digitonin-solubilized supercomplexes at a concentration of 0.2 mg/ml were applied to glow-discharged 400-mesh Quantifoil R1.2/1.3 grids (Quantifoil, Micro Tools GmbH, Germany) coated with a home-made continuous thin layer of carbon. Grids were blotted for 1.5 s and plunged into liquid ethane using an FEI Mark IV Vitrobot operated at 4°C and 100% humidity. High-resolution images were collected on a Titan Krios microscope operated at a voltage of 300 kV with a Falcon II direct electron detector (FEI). Automated single-particle data acquisition was performed with AutoEMation (written by Jianlin Lei), with a nominal magnification of 75,000 × which yields a final pixel size of 1.083 Å at the object scale and with defocus ranging from −1.5 μm to −2.5 μm. A dose rate on the detector was about 38 counts per pixel per second with a total exposure time of 1.3 s. Each micrograph stack contains 21 frames. Eight batches of data were collected with four cryo-samples, obtaining 20,697 micrographs in total.

Image Processing

For Falcon II datasets processing, motion correction at micrograph level was done by the dosefgpu_driftcorr program (written by X. Li) to produce average macrographs over all frames (Li et al., 2013). Micrographs screening, particle picking and normalization were done with EMAN2.1 (Tang et al., 2007) and RELION1.4 (Scheres, 2012). All particles were selected half-manually. The boxing tool 'Swarm' was used to get coordinate files with the suffix 'box'. The particle diameter was set to 380 pixels, and proximity threshold was set to 2.3 to get as many particles as possible. Particles were then extracted using Relion 1.4 with a box size of 480 pixels. Program of CTFFIND3 (Mindell and Grigorieff, 2003) was used to estimate the contrast transfer function parameters. The 2D, 3D classification and refinement were performed with RELION1.4. 1.18 million particles extracted from 13,396 micrographs were subject to a cascade of 2D and 3D classification. Three rounds of 2D classification and one round of 3D classification were performed on four batches of data separately to select the best particles, and 340k particles were left in total. We classified these particles into 3 classes, obtaining models of two different states. 3D auto-refinement was performed on these two sets of particles separately, resulting in resolutions of 4.2 Å and 4.5 Å for each state. We noticed that there were still scattered, blurry or marginalized particles without clearly resolved features in the subsets, so we went back to the 340k particles, and performed another round of 2D and 3D classification. After 3D classification, a set of relatively homogeneous particles (167,761) were subjected to the final refinement, with the 4.0 Å model of porcine $SCI_1III_2IV_1$ which we reported in our previous study low-pass filtered to 60 Å as initial reference. The refinement resulted in an overall structure at a resolution of 7.0 Å, with regions defined by the soft mask being 4.5 Å. A second round of refinement was done by applying an enlarged soft mask of the $SCI_1III_2IV_1$, and improved the resolution to 4.2 Å. Dose weighting process was then performed on micrographs with MotionCor2 (Zheng et al., 2017), which improved the resolution of the $SCI_1III_2IV_1$ to 3.9 Å. The masked refinement procedure was performed to improve the local resolution of our density map. We use Relion software to prepare soft masks. The threshold was set to 0.005. The initial binary mask is extended 3 pixels in all directions, and is further extended with a raised-cosine soft edge of the 5 pixels width. Carefully modified soft masks for CI, the matrix region of CI, the transmembrane region of CI, CIII and CIV were applied to the particle images in 3D auto-refinement process, respectively, giving a better resolution of 3.7, 3.4, 3.7, 3.4 and 9.1 Å for each subregions, respectively. To improve the density map quality of CIV, we classify the 167k particles into four classes with a soft mask of complex IV applied after 3D auto-refine without performing particle aligning. 120k particles from two classes were preserved to reconstruct the structure of CIV, resulting in the reported resolution of CIV to be 5.2 Å within the region defined by the soft mask. Density map of $MCI_2III_2IV_2$ was calculated through a different process. 725k particles were selected after 2D classification. 3D auto-refinement was performed on these subsets of particles. The pixel size was rescaled to 2.16 Å per pixel to speed up the calculation. The angular accuracy information were preserved to calculate a further round of 3D classification without performing the particle alignment. We found that one class containing 7.9k particles showed a higher level of conjunction of complexes. The averaging 3D model low pass filtered to 60 Å was used as the reference for the 3D classification of 64k particles selected from 6 relatively 'bad' classes. Finally, 8.6k particles were selected to perform 3D auto-refine process, resulting in an overall resolution of 17.4 Å for this $MCI_2III_2IV_2$.

Model Building and Refinement

To build atomic models of the *Homo sapiens* CI, we used the 3.6 Å porcine CI structure (PDB code: 5GUP) (Wu et al., 2016) as the initial model. With 3.7 Å CI density map, 3.4 Å map for the matrix region of CI and 3.7 Å CI transmembrane region density map, we were able to model side chains and local geometry to higher accuracy. CI models were adjusted and real-space refined using COOT (Emsley et al., 2010). Finally, all the 14 core subunits and 31 supernumerary subunits were assigned into the 3.7 Å density map. As for

atomic models of human CIII, the 3.6 Å porcine CIII structure (Wu et al., 2016) was chosen as the initial template. Based on 3.4 Å density map, the CIII model was built and refined in the same way as CI. All ligands and phospholipids models were generated using elbow (Moriarty et al., 2009) module in PHENIX (Adams et al., 2010) by their geometric constraints. The ligands and phospholipids were docked into densities and refined using COOT (Emsley and Cowtan, 2004). The $SCI_1III_2IV_1$ density maps were fitted into the $MCI_2III_2IV_2$ in Chimera. All the figures were created by UCSF Chimera (Pettersen et al., 2004) and PyMOL (The PyMOL Molecular Graphics System, Version 1.8 Schrödinger, LLC).

QUANTIFICATION AND STATISTICAL ANALYSIS

All reported resolutions are based on the gold-standard FSC = 0.143 criteria (Scheres and Chen, 2012), and the final FSC curve were corrected for the effect of a soft mask using high-resolution noise substitution (Chen et al., 2013). Final density maps were sharpened by B-factor of -200 $Å^2$ using RELION. Local resolution map was calculated using ResMap (Kucukelbir et al., 2014). The models with the ligands and phospholipids were subjected to global refinement and minimization in real space refinement using PHENIX. FSC curves of the final model versus the summed map and half maps were calculated with the software written by X, Li.

DATA AND SOFTWARE AVAILABILITY

The atomic coordinates of the matrix arm, membrane arm of human CI, CI, CIII, $SCI_1III_2IV_1$ and $MCI_2III_2IV_2$ have been deposited in the Worldwide Protein Data Bank (http://www.rcsb.org): PDB: 5XTB, PDB: 5XTC, PDB: 5XTD, PDB: 5XTE, PDB: 5XTH, and PDB: 5XTI, respectively. The corresponding maps have been deposited in the Electron Microscopy Data Bank (http://emdatabank.org): EMDB: EMD-6771, EMDB: EMD-6772, EMDB: EMD-6773, EMDB: EMD-6774, EMDB: EMD-6775, and EMDB: EMD-6776, respectively.

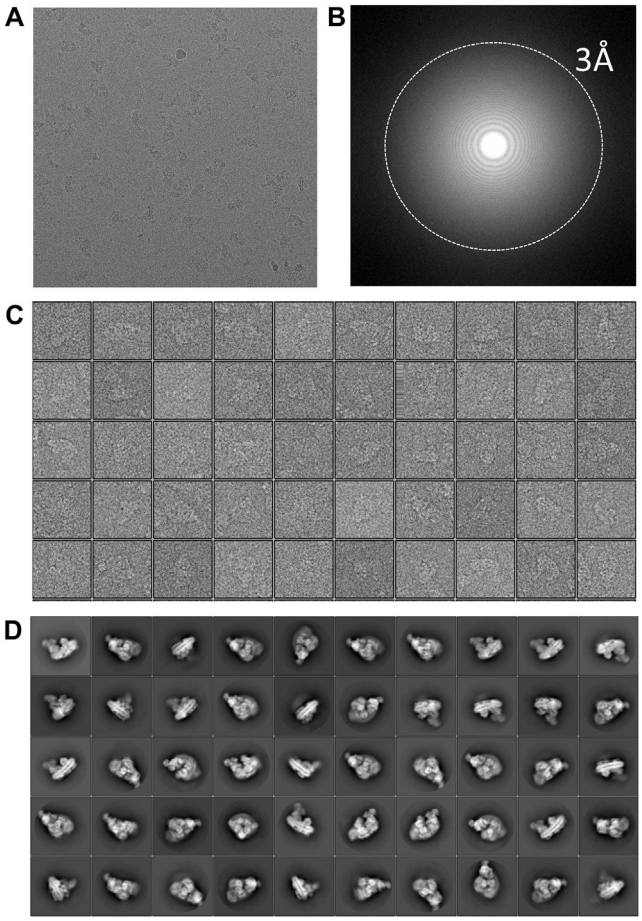

Figure S1. Cryo-EM Analysis of $SCI_1III_2IV_1$, Related to Figure 1 and STAR Methods

(A) A representative cryo-EM micrograph of human $SCI_1III_2IV_1$.

(B) Power-spectrum of the micrograph in (A). The white circle indicates the 3.0-Å frequency.

(C) A collection of raw particles of human $SCI_1III_2IV_1$ collected with Titan Krios (300 kV) and Falcon II.

(D) Representative 2D class averages of different views show fine features of the F-shaped structure.

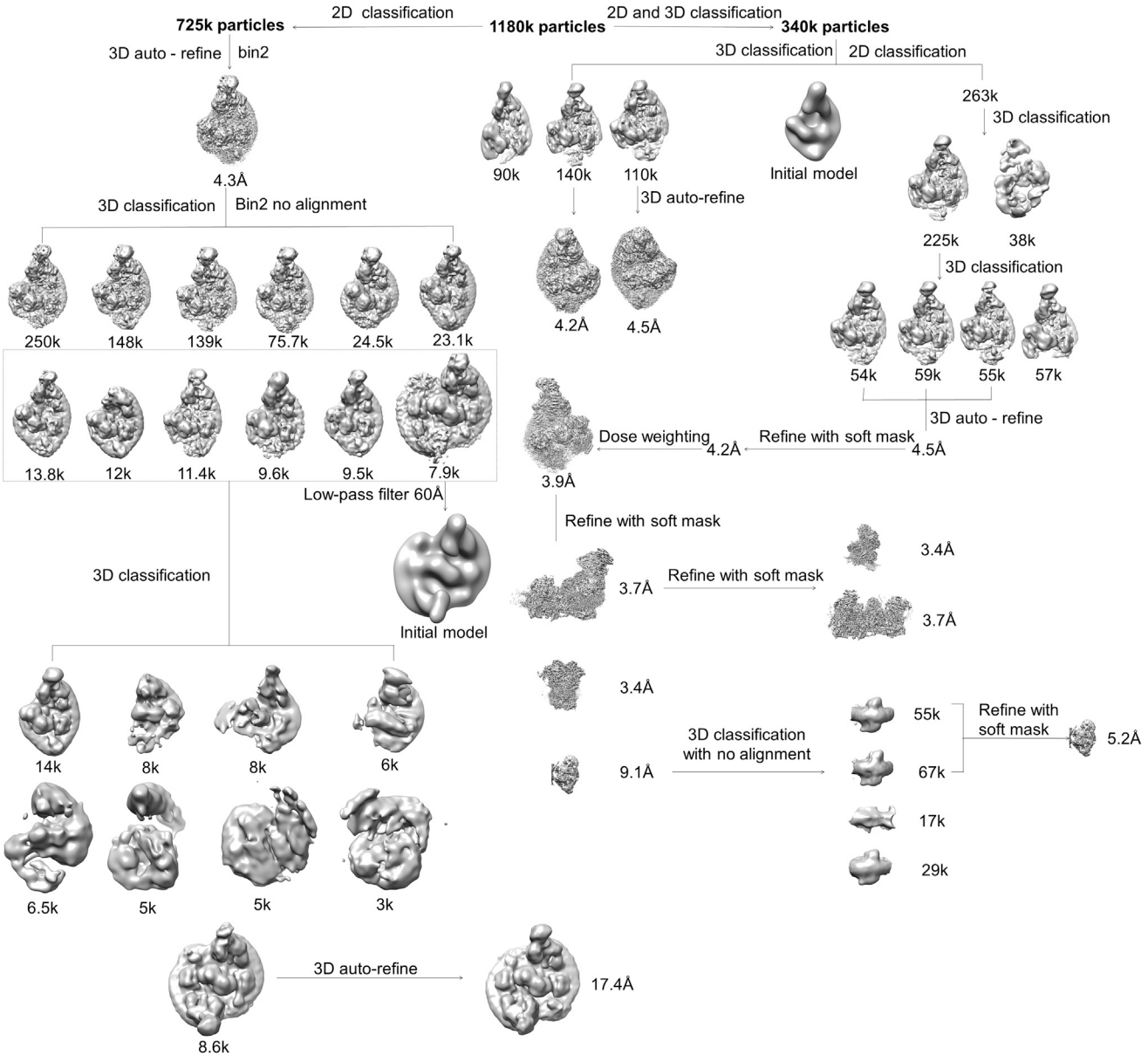

Figure S2. Workflow of 3D Reconstruction with Cryo-EM Data, Related to Figures 1, 2, 3, 4, and 5 and STAR Methods

In the calculation of the human $SCl_1III_2IV_1$, we totally obtained 1,180,000 particles and 340,000 particles were kept after 2D classification, and subject to two rounds of 3D classification. A final dataset containing ~168,000 particles were used for high-resolution refinement and soft masks refinement in different regions. As for $MCl_2III_2IV_2$ density map calculation, 725k particles of all the 1,180,000 particles were selected for 3D auto-refinement. A final dataset containing 8.6k particles were selected to perform 3D auto-refine process (see the STAR Methods for more details).

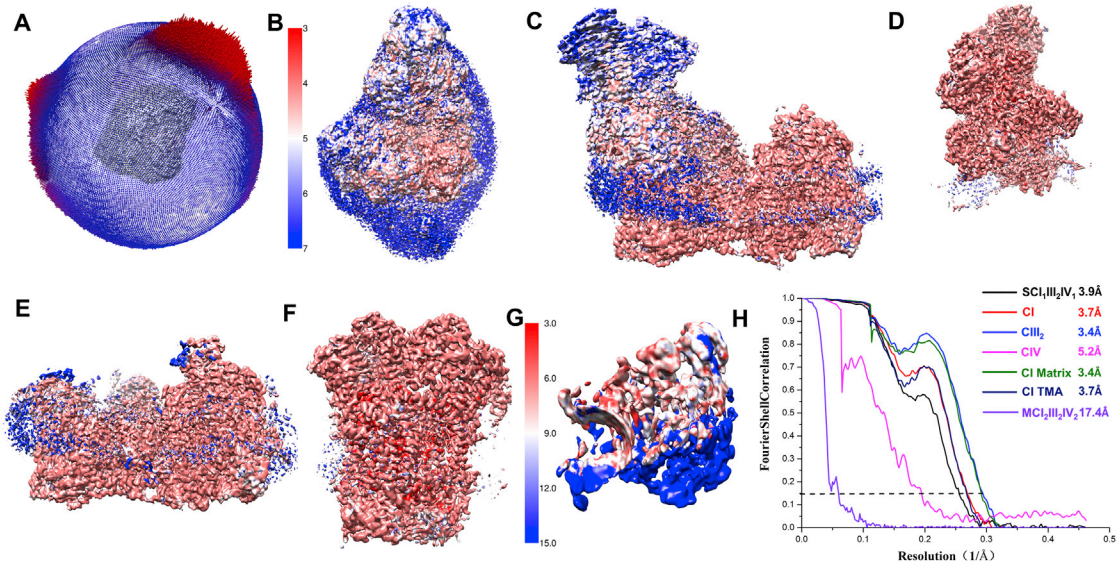

Figure S3. Statistics of the Final Density Maps after Soft Mask Refinement, Related to Figures 1, 2, 3, and 4 and STAR Methods

(A) Particle orientation distributions in the last iteration of the structural refinement. Red cylinders mean more particles on these orientations. Heights of cylinders represent the relative numbers of particles.

(B) Local resolution map of the final 3D density map of human respirasome. Viewed from the matrix region. The color scale from 3.0 −7.0 Å as shown in left. The panels B-F have the same scale as in (B).

(C) Local resolution map of the final 3D density map of human CI. Viewed along the membrane.

(D) Local resolution map of the final 3D density map of matrix arm of human CI. Viewed along the membrane.

(E) Local resolution map of the final 3D density map of the membrane arm of human CI. Viewed along the membrane.

(F) Local resolution map of the final 3D density map of human CIII. Viewed along the membrane.

(G) Local resolution map of the final 3D density map of human CIV. Viewed along the membrane. The color scale from 3.0 −15.0 Å as shown in left.

(H) Gold-standard Fourier Shell Correlation (FSC) curve of the final density maps, after correction of the soft-mask-induced effects. The final resolution of $CI_1III_2IV_1$, CI, CIII2, CIV, CI matrix and CI membrane arm are 3.9, 3.7, 3.4, 5.2, 3.4, 3.7 and 17.4 Å, respectively. TMA, transmembrane arm of CI.

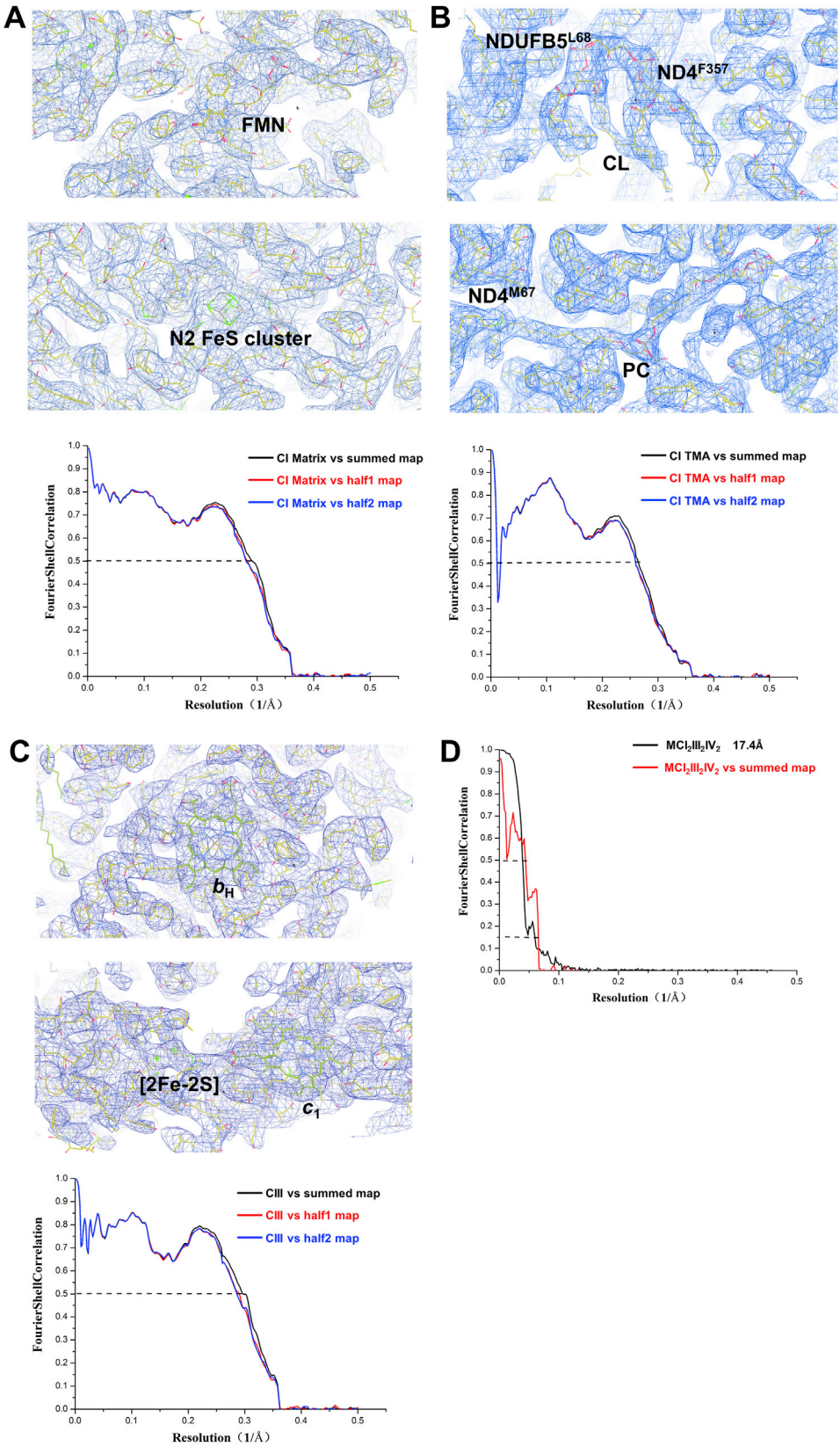

(legend on next page)

Figure S4. Local Resolution Maps of the Final 3D Density Maps, Related to Figures 1, 2, 3, and 4

(A) The density map (blue meshes) of the matrix arm of CI is displayed at rmsd = 13 contour level. The bottom panel shows the FSC curves of the atomic model cross-validation with the summed map and half maps. The backbone is shown in line in Coot.

(B) The density map (blue meshes) of the transmembrane arm of CI is displayed at rmsd = 12 contour level. The bottom panel shows the FSC curves of the atomic model cross-validation with the summed map and half maps. The backbone is shown in line in Coot. TMA, transmembrane arm of CI.

(C) The density map (blue meshes) of CIII is displayed at rmsd = 13 contour level. The bottom panel shows the FSC = 0.5 curves of the atomic model cross-validation with the summed map and half maps. The backbone is shown in line in Coot.

(D) Comparison of the FSC curves of the $MCI_2III_2IV_2$ map with the atomic model cross-validation with the summed map.

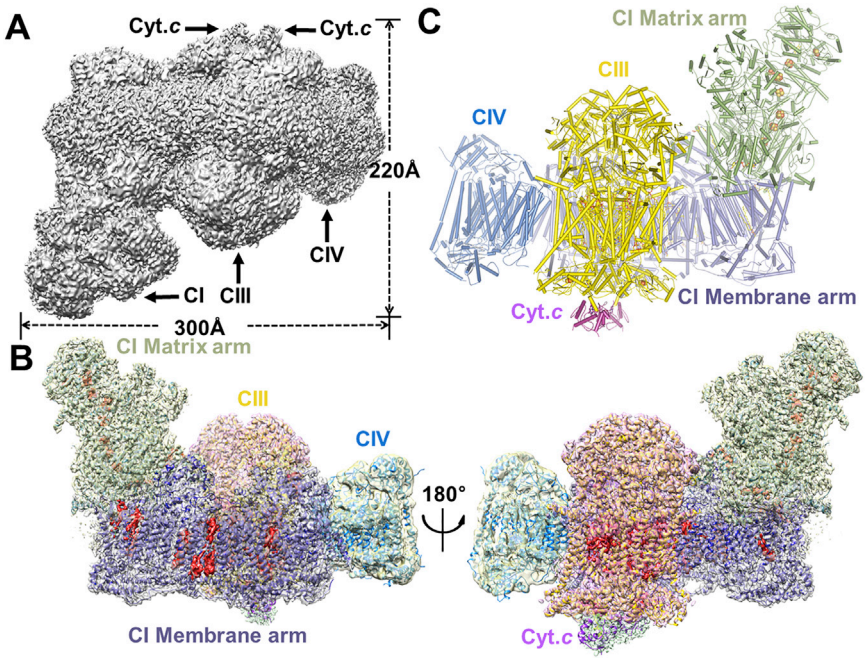

Figure S5. Overall Structure of Human $SCI_1III_2IV_1$, Related to Figures 1, 2, 3, and 4

(A) The side views along the membrane of the density map of human $SCI_1III_2IV_1$ at 3.9 Å (at 3σ contour level) with distinct regions labeled and indicated by black arrows. CI, Complex I; CIII, Complex III; CIV, Complex IV; Cyt.*c*, Cytochrome *c*.

(B) The matrix and membrane arms of CI, CIII, CIV, Cyt.c and cofactors maps with the cartoon presented models after soft mask subregion refinement were aligned to the 3.9 Å map (9σ contour level of CI and CIII; 5σ contour level of CIV, 3σ contour level of Cyt.*c* and 15σ contour level of cofactors) and shown in two differently rotated views along the membrane. The structural models of matrix and membrane arms of CI, CIII, CIV and Cyt.c are colored in green, slate, yellow, marine, and magenta, respectively.

(C) Cartoon representation of the overall structure of human $SCI_1III_2IV_1$ as same colors in (B).

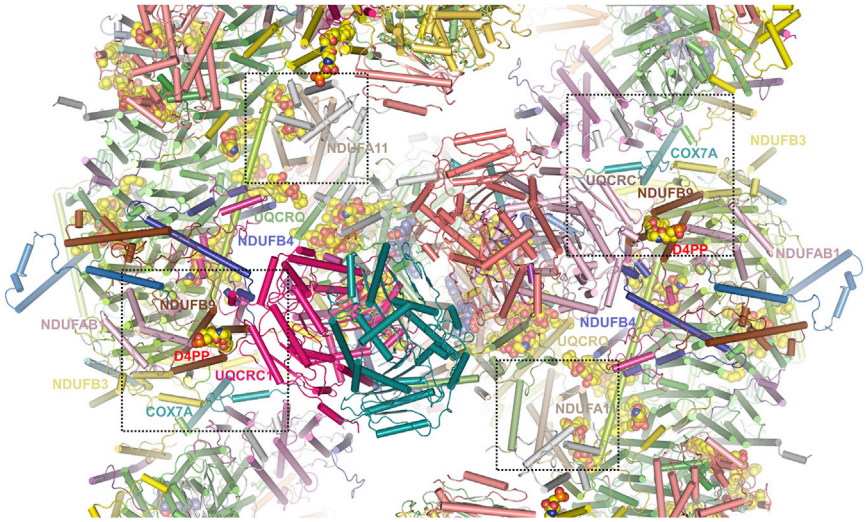

Figure S6. Interactions among CI, CIII, and CIV in Human $MCI_2III_2IV_2$, Related to Figure 6

The interaction regions in human $MCI_2III_2IV_2$ are indicated by the black dash line squares. The image is viewed from the matrix side. Subunits participating in the interactions are colored as labeled with texts in the same colors, respectively. The cofactors are shown in spheres.

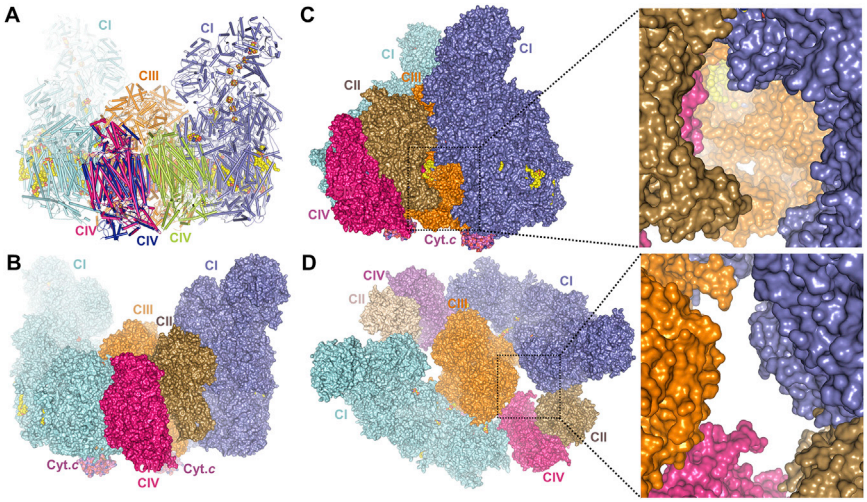

Figure S7. The Organization of All the Respiratory Chain Complexes in ETCS, Related to Figure 7

(A) The structure of the $MCI_2III_2IV_2$ with Cyt.*c* containing CIV dimer structure superposed. The cofactors are shown in spheres. The complexes and Cyt.*c* molecules are colored as labeled with texts in the same colors, respectively.

(B) The proposed model of ETCS. Viewed along the inner membrane. Complex II could insert into the gaps between CI and CIV. All the respiratory chain complexes, cofactors, and loading-state Cyt.*c* molecules are shown in sphere and colored as labeled with texts in the same colors.

(C) The side view of the ETCS model. The right panel shows the adjacent respiratory chain complexes and one of the Q_i binding sites of CIII in ETCS.

(D) The Q-pool in ETCS. Viewed from the matrix side. The right panel shows the Q-pool sealed by CI, CII, CIII and CIV.